PHYSICAL REVIEW B **73**, 214517 (2006)

Magnetic excitations and their anisotropy in $YBa_2Cu_3O_{6+x}$: Slave-boson mean-field analysis of the bilayer *t-J* model

Hiroyuki Yamase and Walter Metzner
Max-Planck-Institute for Solid State Research, Heisenbergstrasse 1, D-70569 Stuttgart, Germany

(Received 3 February 2006; published 15 June 2006)

We perform a comprehensive analysis of the dynamical magnetic susceptibility $\chi(\mathbf{q},\omega)$ in the slave-boson mean-field scheme of the bilayer *t-J* model. We use model parameters appropriate for $YBa_2Cu_3O_{6+x}$ (YBCO), a typical bilayer high-T_c cuprate compound well studied by neutron scattering experiments. In the *d*-wave pairing state, the strongest magnetic spectral weight appears at $\mathbf{q}=\mathbf{Q}\equiv(\pi,\pi)$ and $\omega=\omega_{\mathbf{Q}}^{\mathrm{res}}$, and spreads into a diamond-shaped shell around $\mathbf{Q}$ in $\mathbf{q}$ space for $\omega<\omega_{\mathbf{Q}}^{\mathrm{res}}$. This weight is due to a collective mode, namely a particle-hole bound state, which has a downward ω versus $\mathbf{q}$ dispersion around $\mathbf{Q}$. Within the high intensity shell, the incommensurate (IC) signals at $\mathbf{q}=(\pi,\pi\pm2\pi\eta)$ and $(\pi\pm2\pi\eta,\pi)$ tend to be stronger than the diagonal incommensurate (DIC) signals at $\mathbf{q}=(\pi\pm2\pi\eta',\pi\pm2\pi\eta')$, especially for a large hole density δ. For $\omega\ll\omega_{\mathbf{Q}}^{\mathrm{res}}$ the IC signals completely disappear and the weight remains only around the DIC positions. For $\omega>\omega_{\mathbf{Q}}^{\mathrm{res}}$ strong signals of $\mathrm{Im}\,\chi(\mathbf{q},\omega)$ tracing an upward dispersion are found and interpreted as an overdamped collective excitation near $\omega_{\mathbf{Q}}^{\mathrm{res}}$. In the normal state, $\mathrm{Im}\chi(\mathbf{q},\omega)$ has a broad peak at $\mathbf{q}=\mathbf{Q}$. That is, the IC and DIC signals appear only in the *d*-wave pairing state. We also study effects of a small orthorhombic anisotropy, which is intrinsic in untwinned YBCO crystals. Because of electron-electron correlations favoring *d*-wave shaped Fermi surface deformations, we expect an enhanced anisotropy of magnetic excitation spectra. This effect is particularly pronounced for low δ and at relatively high temperature. The present theory provides a rather detailed microscopic explanation of the most salient properties of magnetic excitations observed in YBCO.

DOI: 10.1103/PhysRevB.73.214517 PACS number(s): 74.25.Ha, 74.72.Bk, 74.20.Mn, 71.10.Fd

I. INTRODUCTION

The undoped parent compounds of high-T_c cuprate superconductors are antiferromagnetic Mott insulators. With carrier doping the antiferromagnetism disappears and a superconducting state with a high transition temperature is realized. Antiferromagnetic (AF) correlations, however, remain even in the superconducting state and the understanding of magnetic properties has been widely recognized as a major issue in the theory of high-T_c cuprates.

Magnetic correlations are directly measured by inelastic neutron scattering experiments. Most of the experiments were performed for the cuprate superconductors $YBa_2Cu_3O_y$ (YBCO) and $La_{2-x}Sr_xCuO_4$ (LSCO). Early studies suggested that YBCO had commensurate antiferromagnetic correlations, that is, the peak signal in the imaginary part of the dynamical magnetic susceptibility $\chi(\mathbf{q},\omega)$ at various frequencies appeared at $\mathbf{q}=\mathbf{Q}\equiv(\pi,\pi)$,[1] while LSCO had incommensurate (IC) correlations in the sense that the peak shifted to $\mathbf{q}=(\pi\pm2\pi\eta,\pi)$ and $(\pi,\pi\pm2\pi\eta)$, where η parametrizes the degree of incommensurability.[2–5] In 1998, measurements with improved resolution revealed that the seemingly commensurate signal of YBCO was actually composed of four peaks at incommensurate wave vectors.[6] Indications for an incommensurate signal in YBCO appeared already in several earlier observations,[7,8] but remained ambiguous due to a limited resolution. The peak positions were identified as $\mathbf{q}=(\pi\pm2\pi\eta,\pi)$ and $(\pi,\pi\pm2\pi\eta)$,[9,10] the same geometry as in LSCO. The IC peaks, however, appeared only below the superconducting transition temperature T_c or possibly below the pseudogap temperature T^*,[6,10–13] in sharp contrast to LSCO, where the IC signals were observed at temperatures well above T_c.[2,14]

The size of the incommensurability η depends on the excitation energy ω. For YBCO, η decreases with increasing ω and vanishes at a specific frequency $\omega_{\mathbf{Q}}^{\mathrm{res}}$. The commensurate, so-called "resonance peak" at $\omega_{\mathbf{Q}}^{\mathrm{res}}$ was extensively investigated for optimally doped[1,15–17] and underdoped samples[16,18–20] before the observation of the IC signals in YBCO. The resonance peak is now regarded to be continuously connected with the IC signals observed at lower frequencies, that is the peak disperses smoothly downwards to lower frequencies when $\mathbf{q}$ is shifted away from $\mathbf{Q}$.[10,11,21,22] Above the resonance energy, possible IC structures were observed.[10] It was recently found that the strongest weight appeared at diagonal incommensurate (DIC) positions $\mathbf{q}=(\pi\pm2\pi\eta,\pi\pm2\pi\eta)$.[23] On the other hand, for LSCO the energy dependence of η was relatively weak compared to YBCO (Ref. 4) and such a robustness of IC structures was often contrasted with the behavior in YBCO. However, recent high energy neutron scattering data for $La_{2-x}Ba_xCuO_4$ with $x=0.125$ revealed that the IC peaks dispersed with ω and merged into a commensurate peak around 55 meV.[24] Above this energy the data showed weak DIC peaks as in YBCO.

Early theoretical work[25–28] pointed out that the differences of magnetic excitations between YBCO and LSCO could be traced back to the difference of the Fermi surface (FS) shape, which we refer to as the fermiology scenario. The FS difference was indeed predicted by LDA band calculations[29–31] and angle-resolved photoemission spectroscopy (ARPES) supported the LDA prediction for YBCO;[32,33] ARPES data for LSCO were not available for a long time. After the experimental observation of IC peaks in YBCO, further detailed calculations[34–40] within the same theoretical frame-

©2006 The American Physical Society

work as in the early days showed that essential features of magnetic excitations in YBCO were captured in the fermiology scenario.

Fermiology theories for LSCO systems were running into problems when ARPES data, first reported in 1999,[41] suggested that the FS of LSCO looks similar to that of YBCO in the doping region below $x \sim 0.15$.[42] If so, fermiology scenarios predict that magnetic excitations should be essentially the same in both YBCO and LSCO, in contradiction with the experimental data. This problem was considered within the slave-boson mean-field scheme of the *t-J* model.[43] It was shown[44] that the model has tendencies toward orientational symmetry breaking of the square lattice symmetry, leading to a *d*-wave shaped FS deformation (*d*FSD): the FS expands along the k_x axis and shrinks along the k_y axis or vice versa. Assuming a coupling to the low temperature tetragonal lattice distortions or their fluctuations, one could understand both the observed FS shape and the structure of magnetic excitations in LSCO consistently.[44–47]

An essentially different picture for magnetic excitations was proposed in 1995,[48] the spin-charge stripe scenario, according to which IC magnetic excitations are mainly controlled by charge-stripe order tendencies in the CuO_2 plane. This scenario is based on the observation of a charge order signal whose wave vector is just twice as large as the IC magnetic wave vector. Although charge order was observed only in a few high-T_c cuprate materials with specific doping rates,[48–51] and in addition the signal was rather weak, the spin-charge stripe scenario attracted much interest.[52]

The spin-charge stripe scenario predicts one-dimensional magnetic signals, that is, IC magnetic peaks should appear either at $\mathbf{q}=(\pi \pm 2\pi\eta, \pi)$ or $(\pi, \pi \pm 2\pi\eta)$. Such a one-dimensional pattern was actually inferred from experiments for partially untwinned YBCO crystals[53] as a strong support for the stripes. However, subsequent neutron scattering studies for almost fully untwinned YBCO[54,55] revealed that magnetic excitations were two-dimensional and had four IC signals. The IC pattern, however, lost fourfold symmetry around $\mathbf{q}=\mathbf{Q}$ and exhibited some anisotropy between the q_x and q_y direction. There are several possible explanations for this anisotropy. (i) The bare band structure effect, due to the orthorhombicity of the crystal structure[56,57] or the CuO chains in YBCO.[58] (ii) The tendency to a *d*FSD due to electron-electron correlations, which enhances the bare anisotropy.[44,59] (iii) Effects of charge stripe fluctuations.[60] The putative charge stripes should be strongly fluctuating to be consistent with the experimental observation that the magnetic signals form a two-dimensional anisotropic geometry.

We focus on the possibility of an enhanced anisotropy due to correlations favoring a *d*FSD. The *d*FSD tendency is generated by forward scattering interactions of electrons close to the FS near $(\pi, 0)$ and $(0, \pi)$. It was first found in the *t-J* model[44] and Hubbard model,[61] and then analyzed in more detail[62–67] and also for other models in various subsequent works.[68–71] If the *d*FSD tendency is very strong, it can lead to a spontaneous breaking of the orientational symmetry of the Fermi surface from tetragonal to orthorhombic. Referring to a stability criterion for Fermi liquids by Pomeranchuk,[72] some authors termed this instability "Pomeranchuk instability."

The *d*FSD competes with *d*-wave singlet pairing.[44,61,63–66] It differs from other frequently discussed ordering tendencies such as antiferromagnetism,[73,74] spin-charge stripes,[48,75] staggered flux,[76] and *d*-density wave,[77] which are driven by interactions with a large momentum transfer near $\mathbf{q}=\mathbf{Q}$, while the *d*FSD is generated from forward scattering. The *d*FSD breaks the orientational symmetry of the square lattice and has the same reduced symmetry as the electronic nematic phase proposed by Kivelson, Fradkin, and Emery.[78] Their route to this phase is, however, not that of a Fermi surface instability, but rather via partial melting of stripe order.

To discuss high-T_c cuprates we should treat both the *d*FSD and the *d*-wave singlet pairing on an equal footing. We use the slave-boson mean-field scheme of the *t-J* model; both tendencies are generated by the *J* term. The *d*FSD tendencies are suppressed by the *d*-wave singlet pairing instability such that no spontaneous Fermi surface symmetry breaking takes place.[44] However, significant *d*FSD correlations survive.[44,66] This correlation effect can drive a sizable enhancement of the Fermi surface anisotropy by a small bare band anisotropy. We analyze this *d*FSD effect on magnetic excitations by using the *anisotropic t-J* model. The idea that *d*FSD correlations may enhance the in-plane anisotropy of magnetic excitations in YBCO has been pursued already in a recent work by Kao and Kee.[59] In that work *d*FSD correlations and pairing are taken into account via a suitable ansatz for the renormalized band structure and the superconducting gap function, while we actually compute these interaction effects, starting from a microscopic model.

Many features of magnetic excitations in YBCO are captured already by the (usual) *isotropic t-J* model. Magnetic excitations in YBCO are well characterized by the bilayer model[7,13,15,17–19,79–81] and therefore have odd and even channels. While most neutron scattering studies were confined to the odd channel so far, recent experiments successfully detected the even channel also.[22,80–85] We perform a comprehensive analysis of magnetic excitations in the bilayer *t-J* model including the above-mentioned *d*FSD effects. We show that prominent features of magnetic excitations of YBCO are well captured in this framework and confirm several theoretical insights obtained earlier. The *d*FSD effect turns out to provide a natural scenario to understand the observed anisotropy of magnetic excitations, especially at low doping and relatively high temperature. Together with previous studies of magnetic excitations in the single layer *t-J* model[27,38,45] and in the bilayer *t-J* model,[38,86] the present study provides a comprehensive understanding of magnetic excitations in YBCO from the fermiology viewpoint. Since the antibonding FS can be easily deformed to be open by *d*FSD correlations, our work is also relevant for the interpretation of ARPES data for untwinned YBCO.

The paper is structured as follows. In Sec. II, we introduce the bilayer *t-J* model and present the slave-boson mean-field scheme. In Sec. III, we discuss self-consistent mean-field solutions of the bilayer system. Section IV is dedicated to magnetic excitations. After a brief qualitative discussion of the dynamical magnetic susceptibility, we present numerical results in two parts: (i) the isotropic case, where comprehensive results are provided to discuss prominent features of magnetic excitations in YBCO, and (ii) the anisotropic case,

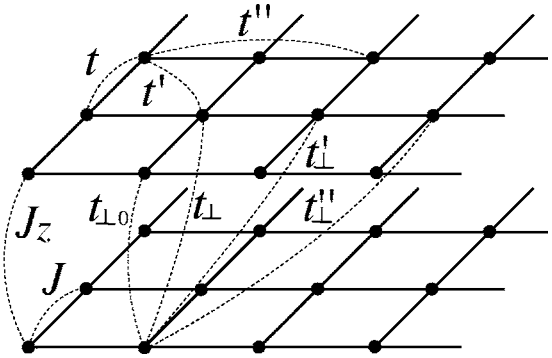

FIG. 1. Notation for superexchange couplings and transfer integrals in the bilayer square lattice model.

where the *d*FSD effect on magnetic excitations is investigated. In Sec. V, we summarize our results through a comparison with experimental data, and conclude in Sec. VI.

II. MODEL AND FORMALISM

We analyze the bilayer *t*-*J* model on a square lattice

$$H = -\sum_{\mathbf{r},\mathbf{r}',\sigma} t_{\mathbf{r}\mathbf{r}'} \tilde{c}^{\dagger}_{\mathbf{r}\sigma}\tilde{c}_{\mathbf{r}'\sigma} + \sum_{\langle \mathbf{r},\mathbf{r}'\rangle} J_{\mathbf{r}\mathbf{r}'}\mathbf{S}_{\mathbf{r}}\cdot\mathbf{S}_{\mathbf{r}'} \tag{1}$$

defined in the Fock space with no doubly occupied sites. The operator $\tilde{c}^{\dagger}_{\mathbf{r}\sigma}$ ($\tilde{c}_{\mathbf{r}\sigma}$) creates (annihilates) an electron with spin σ on site $\mathbf{r}$, while $\mathbf{S}_{\mathbf{r}}$ is the spin operator. The site variable $\mathbf{r}=(x,y,z)$ runs over the bilayer coordinates, that is (x,y) indicates a site on the square lattice and each layer is denoted by $z=0$ or 1. We assume periodic boundary conditions so that $k_z=0$ or π. $J_{\mathbf{r}\mathbf{r}'}$ (>0) is a superexchange coupling between the nearest neighbor sites along each direction, x,y, and z. We take into account hopping amplitudes $t_{\mathbf{r}\mathbf{r}'}$ between $\mathbf{r}$ and $\mathbf{r}'$ up to third-nearest neighbors. We denote $J_{\mathbf{r}\mathbf{r}'}$ and $t_{\mathbf{r}\mathbf{r}'}$ by using the conventional notation defined in Fig. 1.

We introduce the slave particles, $f_{\mathbf{r}\sigma}$ and $b_{\mathbf{r}}$, as $\tilde{c}_{\mathbf{r}\sigma} = b^{\dagger}_{\mathbf{r}} f_{\mathbf{r}\sigma}$, where $f_{\mathbf{r}\sigma}$ ($b_{\mathbf{r}}$) is a fermion (boson) operator that carries spin σ (charge e), and $\mathbf{S}_{\mathbf{r}} = \frac{1}{2} f^{\dagger}_{\mathbf{r}\alpha}\boldsymbol{\sigma}_{\alpha\beta} f_{\mathbf{r}\beta}$ with the Pauli matrices $\boldsymbol{\sigma}=(\sigma^x,\sigma^y,\sigma^z)$. The slave bosons and fermions are linked by the local constraint $b^{\dagger}_{\mathbf{r}}b_{\mathbf{r}} + \Sigma_{\sigma} f^{\dagger}_{\mathbf{r}\sigma} f_{\mathbf{r}\sigma} = 1$. This is an exact transformation known as the slave-boson formalism. We then decouple the interaction with the so-called resonating-valence-bond (RVB) mean fields:[43] $\chi_{\tau} \equiv \langle \Sigma_{\sigma} f^{\dagger}_{\mathbf{r}\sigma} f_{\mathbf{r}'\sigma}\rangle, \langle b^{\dagger}_{\mathbf{r}} b_{\mathbf{r}'}\rangle$, and $\Delta_{\tau} \equiv \langle f_{\mathbf{r}\uparrow} f_{\mathbf{r}'\downarrow} - f_{\mathbf{r}\downarrow} f_{\mathbf{r}'\uparrow}\rangle$, with $\boldsymbol{\tau} = \mathbf{r}' - \mathbf{r}$. These mean fields are assumed to be real constants independent of sites $\mathbf{r}$. We approximate the bosons to condense at the bottom of the band, which is reasonable at low temperature and leads to $\langle b^{\dagger}_{\mathbf{r}} b_{\mathbf{r}'}\rangle = \delta$, where δ is the hole density. The resulting Hamiltonian reads

$$H_0 = \sum_{\mathbf{k}} \left(f^{\dagger}_{\mathbf{k}\uparrow} f_{-\mathbf{k}\downarrow} \right) \begin{pmatrix} \xi_{\mathbf{k}} & -\Delta_{\mathbf{k}} \\ -\Delta_{\mathbf{k}} & -\xi_{\mathbf{k}} \end{pmatrix} \begin{pmatrix} f_{\mathbf{k}\uparrow} \\ f^{\dagger}_{-\mathbf{k}\downarrow} \end{pmatrix}, \tag{2}$$

with a global constraint $\Sigma_{\sigma}\langle f^{\dagger}_{\mathbf{r}\sigma} f_{\mathbf{r}\sigma}\rangle = 1-\delta$; the $\mathbf{k}$ summation is over $|k_{x(y)}| \le \pi$, and $k_z=0$ and π. Here $\xi_{\mathbf{k}} = \epsilon^{\parallel}_{\mathbf{k}} + \epsilon^{\perp}_{\mathbf{k}} - \mu$, with the in-plane ($c$-axis) dispersion $\epsilon^{\parallel}_{\mathbf{k}}$ ($\epsilon^{\perp}_{\mathbf{k}}$), and $\Delta_{\mathbf{k}} = \Delta^{\parallel}_{\mathbf{k}} + \Delta^{\perp}_{\mathbf{k}}$, with the singlet pairing gap in (out of) the plane $\Delta^{\parallel}_{\mathbf{k}}$ ($\Delta^{\perp}_{\mathbf{k}}$); μ is the chemical potential. The explicit momentum dependence of the dispersion is given by

$$\begin{aligned}\epsilon^{\parallel}_{\mathbf{k}} = &-2\Big[\left(t_x\delta + \tfrac{3}{8}J_x\chi_x\right)\cos k_x + \left(t_y\delta + \tfrac{3}{8}J_y\chi_y\right)\cos k_y \\ &+ 2t'\delta\cos k_x\cos k_y + t''_x\delta\cos 2k_x + t''_y\delta\cos 2k_y\Big],\end{aligned} \tag{3}$$

$$\begin{aligned}\epsilon^{\perp}_{\mathbf{k}} = &-\Big[\left(t_{\perp 0}\delta + \tfrac{3}{8}J_z\chi_z\right) + 2(t_{\perp x}\delta\cos k_x + t_{\perp y}\delta\cos k_y \\ &+ 2t'_{\perp}\delta\cos k_x\cos k_y + t''_{\perp x}\delta\cos 2k_x \\ &+ t''_{\perp y}\delta\cos 2k_y)\Big]\cos k_z,\end{aligned} \tag{4}$$

and that of the gap function by

$$\Delta^{\parallel}_{\mathbf{k}} = -\tfrac{3}{4}(J_x\Delta_x\cos k_x + J_y\Delta_y\cos k_y), \tag{5}$$

$$\Delta^{\perp}_{\mathbf{k}} = -\tfrac{3}{8}J_z\Delta_z\cos k_z. \tag{6}$$

In the bilayer high-T_c cuprates, a $(\cos k_x - \cos k_y)^2$-type c-axis dispersion was computed[87] and actually observed in $Bi_2Sr_2CaCu_2O_{8+\delta}$.[88,89] To adapt Eq. (4) to this behavior, we choose transverse hopping amplitudes as follows: $t_{\perp 0} = [(\gamma_x^2 + \gamma_y^2)/2]t_z$, $t_{\perp x} = t_{\perp y} = 0$, $t'_{\perp} = -(\gamma_x\gamma_y/2)t_z$, $t''_{\perp x} = (\gamma_x^2/4)t_z$, and $t''_{\perp y} = (\gamma_y^2/4)t_z$. The parameters γ_x and γ_y allow for a convenient parametrization of an in-plane anisotropy as specified below. The resulting c-axis dispersion reads

$$\epsilon^{\perp}_{\mathbf{k}} = -\left[t_z\delta(\gamma_x\cos k_x - \gamma_y\cos k_y)^2 + \tfrac{3}{8}J_z\chi_z\right]\cos k_z, \tag{7}$$

which has the expected form in the isotropic case $\gamma_x = \gamma_y = 1$.

$YBa_2Cu_3O_y$ has an orthorhombic crystal structure for $y \ge 6.4$, where the superconducting state is realized at low T.[90] Such orthorhombicity yields xy anisotropy, which we incorporate by introducing a single parameter α as follows:

$$t_x = t(1+\alpha/2), \quad t_y = t(1-\alpha/2), \tag{8}$$

$$J_x = J(1+\alpha), \quad J_y = J(1-\alpha), \tag{9}$$

$$t''_x = t''(1+\alpha/2), \quad t''_y = t''(1-\alpha/2), \tag{10}$$

$$\gamma_x = 1+\alpha/4, \quad \gamma_y = 1-\alpha/4. \tag{11}$$

With this parametrization, $t_{x(y)}$, $t''_{x(y)}$, and $t''_{\perp x(y)}$ have the same degree of xy anisotropy, while the anisotropy of $J_{x(y)}$ is twice as large, as imposed by the superexchange mechanism.

We determine χ_{τ} and Δ_{τ} with $\tau = x,y,z$ by solving the following self-consistency equations numerically:

$$\chi_{\tau} = -\frac{1}{N}\sum_{\mathbf{k}} \cos k_{\tau}\frac{\xi_{\mathbf{k}}}{E_{\mathbf{k}}}\tanh\frac{E_{\mathbf{k}}}{2T}, \tag{12}$$

$$\Delta_{\tau} = -\frac{1}{N}\sum_{\mathbf{k}} \cos k_{\tau}\frac{\Delta_{\mathbf{k}}}{E_{\mathbf{k}}}\tanh\frac{E_{\mathbf{k}}}{2T}, \tag{13}$$

$$\delta = \frac{1}{N}\sum_{\mathbf{k}} \frac{\xi_{\mathbf{k}}}{E_{\mathbf{k}}}\tanh\frac{E_{\mathbf{k}}}{2T}, \tag{14}$$

where $E_{\mathbf{k}} = \sqrt{\xi_{\mathbf{k}}^2 + \Delta_{\mathbf{k}}^2}$ and N is the total number of (bilayer) lattice sites.

III. SELF-CONSISTENT SOLUTION

The material dependence of high-T_c cuprates is mainly taken into account by different choices of band parameters.[26,91–93] We use the following parameters for YBCO:

$$t/J = 2.5, \quad t'/t = -0.3, \quad t''/t = 0.15, \quad J_z/J = 0.1,$$
$$t_z/t = 0.15, \quad \text{and} \quad \alpha = -0.05.$$

This choice has been done judiciously. *Ab initio* calculations[94] indicate that realistic values for t/J lie in the range 2–5. Even within this restricted interval, we found that the behavior of Im $\chi(\mathbf{q},\omega)$ strongly depends on the choice of t/J. We have chosen t/J in such a way that the energy of the resonance mode at $\mathbf{q}=(\pi,\pi)$ is maximal at optimal doping, that is near $\delta=0.15$ (see Fig. 10), to roughly agree with experiments.[12,13,81,84] The ratios t'/t and t''/t are extracted from an LDA band calculation for YBCO.[87] The value of J_z/J is fixed rather uniquely by the optical magnon energy in YBCO.[95,96] The bilayer system has two FSs, the bonding band FS and the antibonding band FS. With increasing δ, the latter can change from a holelike FS to an electronlike FS in the region we are interested in. The hole density at which such a FS topology change occurs strongly depends on t_z. With our choice of t_z/t, which is a bit larger than LDA estimates,[87] the antibonding FS becomes electronlike for $\delta \gtrsim 0.20$. Some ARPES data for $Bi_2Sr_2CaCu_2O_{8+\delta}$ indeed suggest an electronlike antibonding FS for sufficiently high overdoping.[89,97] ARPES data for YBCO with such a high doping are not yet available.

It is not easy to determine the anisotropy parameter α; even its sign is not obvious. The orthorhombic YBCO has a lattice constant anisotropy $a<b$, where $a(b)$ is the lattice constant along the $x(y)$ direction. This contributes to an enhancement of t_x. On the other hand, YBCO contains CuO chains along the y direction. A small hybridization with the chain band enhances t_y, an effect opposite to the lattice constant effect. If one estimates a band anisotropy from the predicted FSs in Ref. 87, a small negative α is obtained. A most recent LDA calculation supports this estimate and predicts that t_y is larger than t_x by about 3%–4%.[98] Hence we assume $t_x<t_y$ and set $\alpha=-0.05$ when analyzing the in-plane anisotropy of Im $\chi(\mathbf{q},\omega)$. We will also present results for the isotropic case, $\alpha=0$, for comparison.

We introduce the following convenient notation:

$$\chi_0 = \frac{\chi_x + \chi_y}{2}, \quad \chi_d = \frac{\chi_x - \chi_y}{2}, \tag{15}$$

$$\Delta_d = \frac{\Delta_x - \Delta_y}{2}, \quad \Delta_s = \frac{\Delta_x + \Delta_y}{2}, \tag{16}$$

where χ_d is an order parameter of the dFSD, and Δ_d (Δ_s) is the d-wave (s-wave) in-plane singlet pairing amplitude; we choose $\Delta_x \geq 0$.

For $\alpha=0$, there is no dFSD,[44,66] that is, $\chi_d=0$, and an isotropic d-wave pairing state is stabilized at low T, that is, $\Delta_s=\Delta_z=0$. Note that a finite Δ_z contributes to an s-wave pairing component of $\Delta_\mathbf{k}$ [see Eq. (6)]. The temperature dependences of χ_0, χ_z, and Δ_d are shown in Fig. 2(a) and their δ dependences in Fig. 2(b). χ_0 and χ_z depend very weakly on T. In particular, the onset of Δ_d does not affect χ_0 and χ_z substantially. At $\delta=0$, χ_z becomes zero, that is, the layers are decoupled regardless of the interlayer coupling J_z in the present mean-field framework, where antiferromagnetic order is not taken into account. The layers couple weakly only for finite δ. The d-wave pairing amplitude Δ_d increases with decreasing δ, which however should not be interpreted as an enhancement of a superconducting order parameter at lower δ, but rather as the increase of a one-particle pseudogap energy scale in the slave-boson mean-field scheme.[43]

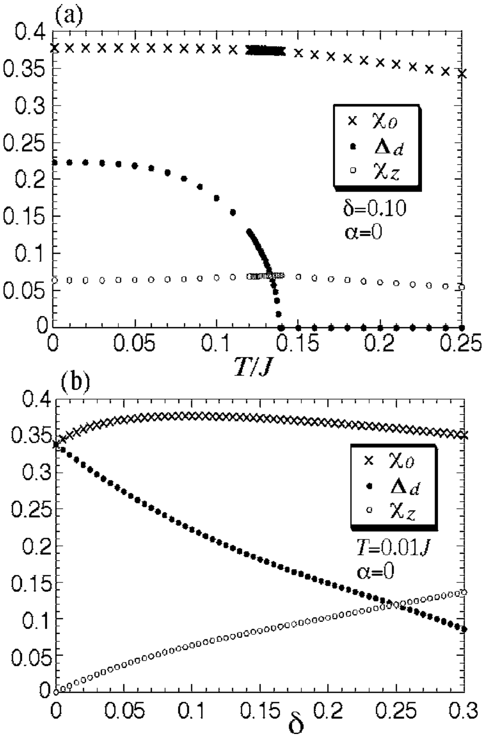

FIG. 2. Mean fields χ_0, Δ_d, and χ_z for $\alpha=0$: (a) T dependence for $\delta=0.10$ and (b) δ dependence at $T=0.01J$.

When the anisotropy parameter α is introduced, the system loses tetragonal symmetry, and χ_d, Δ_s, and Δ_z can become finite. Since the temperature and doping dependences of χ_0, Δ_d, and χ_z for $\alpha=-0.05$ are almost the same as in Fig. 2, we focus on χ_d, Δ_s, and Δ_z. The temperature dependences of χ_d, Δ_s, and Δ_z are shown in Fig. 3(a). χ_d increases with decreasing T, which is due to the development of dFSD correlations, and exhibits a cusp at the onset of singlet pairing, which is denoted as T_{RVB} in the slave-boson theory; note that Δ_d, Δ_z, and Δ_s have the same onset temperature. Below T_{RVB}, dFSD correlations are suppressed leading to a suppression of χ_d. But χ_d saturates at a finite value at zero temperature and is still enhanced compared to χ_d at high T. Since the renormalized band is mainly characterized by the renormalized nearest-neighbor hopping $\bar{t}_\tau = t_\tau\delta + \frac{3}{8}J_\tau\chi_\tau$ [Eq. (3)], this enhancement contributes to the band anisotropy. Defining $\Delta\bar{t} = |\bar{t}_x - \bar{t}_y|/2$ and $\bar{t}_0 = (\bar{t}_x + \bar{t}_y)/2$, we plot $2\Delta\bar{t}/\bar{t}_0$ in Fig. 3(b) for several choices of δ. Although the bare anisotropy is only 5%, the renormalized band anisotropy is enhanced up to around 25% for $\delta=0.08$ by dFSD correlations. The enhancement is less prominent at higher δ.

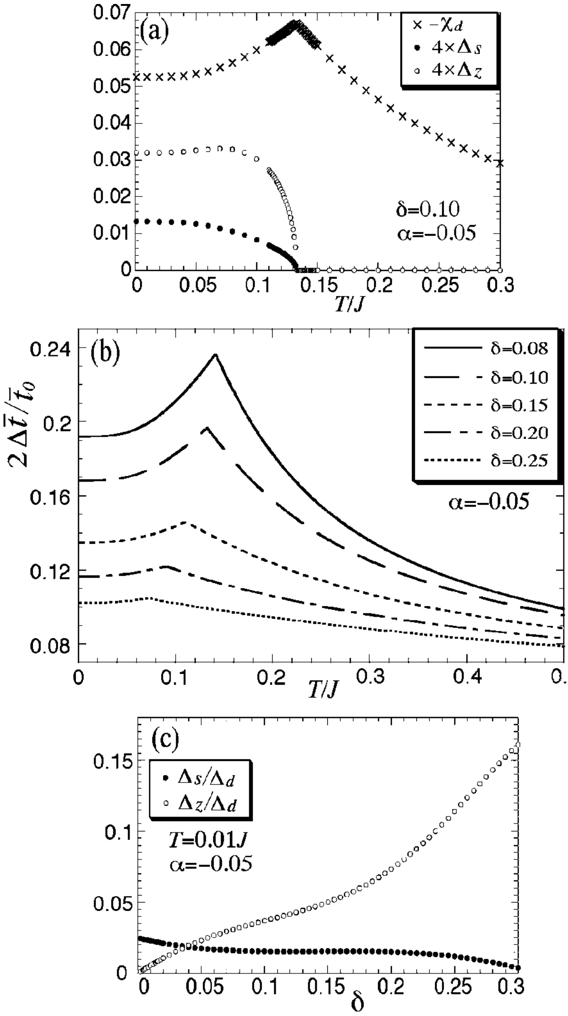

FIG. 3. (a) T dependence of χ_d, Δ_s, and Δ_z for $\delta=0.10$ and $\alpha=-0.05$; Δ_s and Δ_z are multiplied by 4; note that $\chi_d<0$ because of $\alpha<0$. (b) T dependence of anisotropy of the renormalized band, $2\Delta\bar{t}/\Delta\bar{t}_0$, for several choices of δ. (c) δ dependence of Δ_s and Δ_z at $T=0.01J$.

Figure 3(c) shows the doping dependences of Δ_s and Δ_z at low T. Although Δ_s increases at lower δ, its magnitude remains very small compared to Δ_d. Note that we obtain a positive Δ_s for $\alpha=-0.05$, that is $\Delta_x>|\Delta_y|$ for $J_x<J_y$, which means that the s-wave component reduces the anisotropy of $|\Delta_{\mathbf{k}}^{\parallel}|$ caused by the anisotropy of J [see Eq. (5)]. The out-of-plane pairing Δ_z becomes finite at finite δ. Its sign is determined uniquely through the linear coupling to Δ_d. It becomes positive for the present band parameters. In the antibonding band ($k_z=\pi$), Δ_z enhances the magnitude of $\Delta_{\mathbf{k}}$ at $(\pi,0)$ and reduces it at $(0,\pi)$, and vice versa in the bonding band ($k_z=0$).

The FS at low T, which we define by $\xi_{\mathbf{k}}=0$ in the singlet pairing state, is shown in Figs. 4(a)–4(c) for several choices of δ. The bonding band ($k_z=0$) forms the outer FS and the antibonding band ($k_z=\pi$) the inner FS. For $\alpha=0$, the inner FS changes into an electronlike FS for $\delta\gtrsim0.20$ while the outer FS stays holelike. For $\alpha=-0.05$, the inner FS becomes open for all δ in Fig. 4. The inner FS always opens already for a tiny anisotropy parameter for doping around $\delta\approx0.20$, since the original inner FS is close to $(\pi,0)$ and $(0,\pi)$ in this case. It depends sensitively on the size of α whether an open FS is realized at low δ where dFSD correlations become large but the original inner FS is away from $(\pi,0)$ and $(0,\pi)$. The antibonding band and the bonding band have different hole densities, δ_a and δ_b, respectively, as shown in Fig. 5. From the inset of Fig. 5 we see that the antibonding band has a hole density more than 1.5 times higher than the total (average) hole density δ.

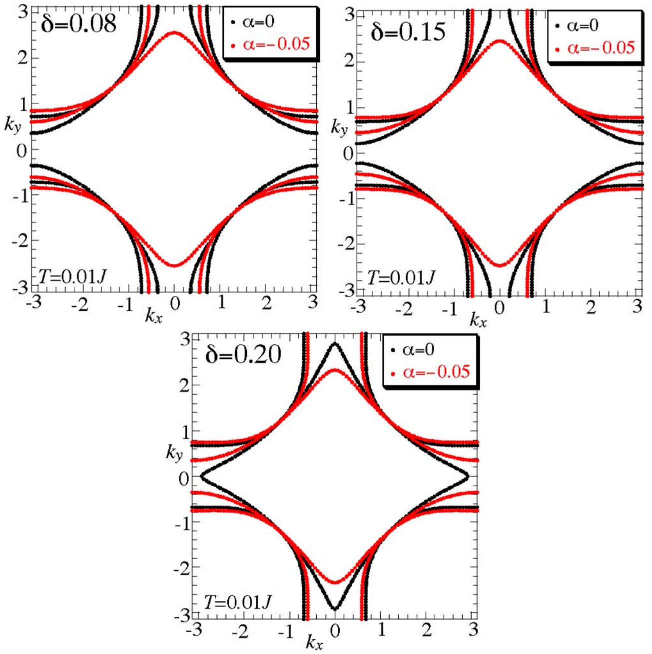

FIG. 4. (Color online) Fermi surfaces for several choices of δ at low T for $\alpha=0$ (black lines) and $\alpha=-0.05$ (red/dark gray lines).

IV. MAGNETIC EXCITATIONS

Next we investigate magnetic excitation spectra in the bilayer t-J model using the self-consistent mean-field solutions. The irreducible dynamical magnetic susceptibility $\chi_0(\mathbf{q},\omega)$ is given by

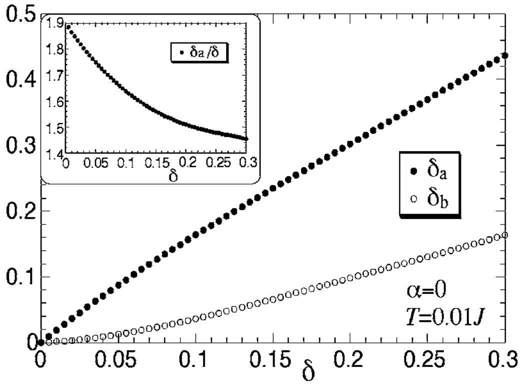

FIG. 5. Hole density in the antibonding band (δ_a) and the bonding band (δ_b) as a function of total hole density δ; note that $\delta=(\delta_a+\delta_b)/2$. The inset shows the ratio δ_a/δ.

$$\begin{aligned}\chi_0(\mathbf{q},\omega) = \frac{1}{4N}\sum_{\mathbf{k}}\Bigg[& C^{+}_{\mathbf{k},\mathbf{k+q}}\left(\tanh\frac{E_{\mathbf{k}}}{2T} - \tanh\frac{E_{\mathbf{k+q}}}{2T}\right) \\ & \times\frac{1}{E_{\mathbf{k}} - E_{\mathbf{k+q}} + \omega + i\Gamma} \quad + \frac{1}{2}C^{-}_{\mathbf{k},\mathbf{k+q}} \\ & \times\left(\tanh\frac{E_{\mathbf{k}}}{2T} + \tanh\frac{E_{\mathbf{k+q}}}{2T}\right)\times\quad\left(\frac{1}{E_{\mathbf{k}} + E_{\mathbf{k+q}} + \omega + i\Gamma}\right. \\ & \left.\left. + \frac{1}{E_{\mathbf{k}} + E_{\mathbf{k+q}} - \omega - i\Gamma}\right)\right)\Bigg], \end{aligned} \tag{17}$$

where Γ is a positive infinitesimal and

$$C^{\pm}_{\mathbf{k},\mathbf{k+q}} = \frac{1}{2}\left(1 \pm \frac{\xi_{\mathbf{k}}\xi_{\mathbf{k+q}} + \Delta_{\mathbf{k}}\Delta_{\mathbf{k+q}}}{E_{\mathbf{k}}E_{\mathbf{k+q}}}\right). \tag{18}$$

Note that the k_z component of $\mathbf{k}$ is summed only over the two values $k_z = 0$ and π, corresponding to a bonding and an antibonding band, respectively. Particle-hole scattering processes are therefore intraband processes for $q_z = 0$ and interband processes for $q_z = \pi$. The former is called the even channel and the latter the odd channel.

In a renormalized random phase approximation (RPA)[34,99] the dynamical magnetic susceptibility $\chi(\mathbf{q},\omega)$ is given by

$$\chi(\mathbf{q},\omega) = \frac{\chi_0(\mathbf{q},\omega)}{1 + J(\mathbf{q})\chi_0(\mathbf{q},\omega)}, \tag{19}$$

where

$$J(\mathbf{q}) = 2r(J_x \cos q_x + J_y \cos q_y) + J_z \cos q_z \tag{20}$$

with a renormalization factor r. In the plain RPA one has $r = 1$, which leads to a divergence of $\chi(\mathbf{q},0)$ at $\mathbf{q} \approx (\pi,\pi,\pi)$ in a wide doping region ($\delta \lesssim 0.20$), signaling an instability toward the AF state. However, several numerical studies of the *t-J* model indicate that the antiferromagnetic instability is overestimated by the RPA.[74,100,101] Fluctuations not included in RPA obviously suppress the instability. This can be taken into account in a rough and phenomenological way by setting $r < 1$.[34,99] Here we choose the value $r = 0.5$, which confines the AF instability to $\delta \lesssim 0.064$, consistent with actual YBCO samples.[90,102]

In the following we will frequently specify q_z by referring to the "even" or "odd" channel, and include only the remaining q_x and q_y variables in $\mathbf{q}$.

A. Basic properties

Before calculating the dynamical magnetic susceptibility numerically, we first discuss generic properties of $\mathrm{Im}\,\chi(\mathbf{q},\omega)$, which hold in both odd and even channels. At zero temperature the *d*-wave superconducting state is realized and

$$\mathrm{Im}\,\chi_0(\mathbf{q},\omega) = \frac{\pi}{4N}\sum_{\mathbf{k}} C^{-}_{\mathbf{k},\mathbf{k+q}}\delta(E_{\mathbf{k}} + E_{\mathbf{k+q}} - \omega). \tag{21}$$

Hence, $\mathrm{Im}\,\chi_0(\mathbf{q},\omega)$ has a threshold energy defined by

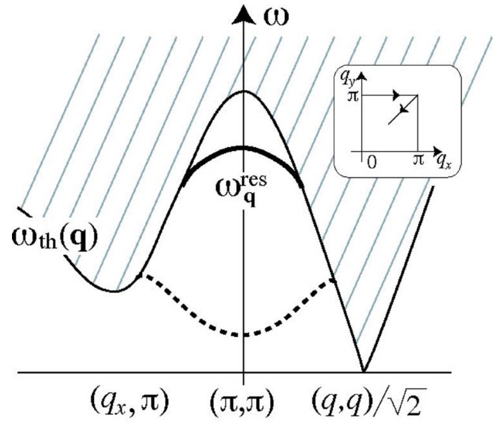

FIG. 6. (Color online) Schematic plot of magnetic excitation spectra $\mathrm{Im}\,\chi(\mathbf{q},\omega)$; the $\mathbf{q}$ directions are shown in the inset. The hatched region represents the continuum spectrum and its lower edge is $\omega_{\mathrm{th}}(\mathbf{q})$. The bold solid line $\omega^{\mathrm{res}}_{\mathbf{q}}$ represents a typical dispersion of the collective mode. The mode is softened near the AF instability leading to an upward dispersion as shown by the dotted line.

$$\omega_{\mathrm{th}}(\mathbf{q}) = \min\{E_{\mathbf{k}} + E_{\mathbf{k+q}}, \mathbf{k} \in \mathrm{BZ}\}, \tag{22}$$

above which continuum excitations start. $\omega_{\mathrm{th}}(\mathbf{q})$ is sketched by the solid line in Fig. 6 and has a maximum at $\mathbf{q} = \mathbf{Q}$. Along the diagonal direction $\mathbf{q} = (q,q)/\sqrt{2}$, gapless excitations appear, which are due to scattering processes between the *d*-wave gap nodes.

The denominator in Eq. (19) vanishes if both real and imaginary parts vanish, that is

$$1 + J(\mathbf{q})\mathrm{Re}\,\chi_0(\mathbf{q},\omega^{\mathrm{res}}_{\mathbf{q}}) = 0, \tag{23}$$

$$\mathrm{Im}\,\chi_0(\mathbf{q},\omega^{\mathrm{res}}_{\mathbf{q}}) = 0. \tag{24}$$

As widely discussed in the literature,[34,36,38–40,58,103–106] Eqs. (23) and (24) can be simultaneously satisfied when $\mathrm{Im}\,\chi_0(\mathbf{q},\omega)$ jumps from zero to a finite value at $\omega = \omega_{\mathrm{th}}(\mathbf{q})$, which gives rise to a logarithmic divergence of $\mathrm{Re}\,\chi_0(\mathbf{q},\omega)$, such that there is always a solution $\omega = \omega^{\mathrm{res}}_{\mathbf{q}} < \omega_{\mathrm{th}}(\mathbf{q})$. This solution describes an in-gap collective mode of particle-hole excitations with spin 1 and charge zero. Note that $\mathbf{q}$ is not restricted to $\mathbf{Q}$. In fact, the collective mode appears also around $\mathbf{q} = \mathbf{Q}$, in particular at IC or DIC wave vectors as sketched in Fig. 6. Expanding $J(\mathbf{q})\mathrm{Re}\,\chi_0(\mathbf{q},\omega)$ around $\mathbf{q} = \mathbf{Q}$ and $\omega = \omega^{\mathrm{res}}_{\mathbf{Q}}$, we obtain the asymptotic form of the dispersion

$$\omega^{\mathrm{res}}_{\mathbf{q}} = \omega^{\mathrm{res}}_{\mathbf{Q}} - \frac{1}{2}\left[\frac{(q_x - \pi)^2}{m_x} + \frac{(q_y - \pi)^2}{m_y}\right], \tag{25}$$

where

$$m_{x(y)}^{-1} = [J(\mathbf{Q})]^{-1} \times \frac{\partial^2 J(\mathbf{q})\mathrm{Re}\,\chi_0(\mathbf{q},\omega)}{\partial q_{x(y)}^2} \Bigg/ \frac{\partial\,\mathrm{Re}\,\chi_0(\mathbf{q},\omega)}{\partial \omega}\Bigg|_{\mathbf{q}=\mathbf{Q},\omega=\omega_{\mathbf{Q}}^{\mathrm{res}}}. \tag{26}$$

The denominator in Eq. (26) is usually positive for $\omega < \omega_{\mathrm{th}}(\mathbf{Q})$. The numerator is expected to be negative close to the commensurate AF instability since $|J(\mathbf{q})\mathrm{Re}\,\chi_0(\mathbf{q},\omega)|$ has a commensurate peak and $J(\mathbf{q})<0$, leading to an upward dispersion (dotted line in Fig. 6). With hole doping, the peak of $|J(\mathbf{q})\mathrm{Re}\,\chi_0(\mathbf{q},\omega)|$ usually shifts to IC positions, and thus its curvature at $\mathbf{q}=\mathbf{Q}$ becomes positive, that is, $\omega_{\mathbf{q}}^{\mathrm{res}}$ has a downward dispersion (bold solid line in Fig. 6). When the collective mode mixes with the continuum, it disappears due to overdamping.

The infinitesimal Γ in Eq. (17) is replaced by a finite small value in numerical calculations, leading to a cutoff of the logarithmic divergence of $\mathrm{Re}\,\chi_0(\mathbf{q},\omega)$. A similar cutoff occurs also for finite T. Then Eq. (23) can be satisfied only when $\mathrm{Im}\,\chi_0(\mathbf{q},\omega)$ has a sufficiently large jump at $\omega=\omega_{\mathrm{th}}(\mathbf{q})$ or when $\mathrm{Re}\,\chi_0(\mathbf{q},\omega)$ is sufficiently large; the latter is always the case near the AF instability. Practically therefore the collective mode is well defined only in a limited momentum region (Fig. 6). Moreover, since $\mathrm{Im}\,\chi_0(\mathbf{q},\omega)$ becomes finite for a finite Γ or a finite T, the collective mode has a finite lifetime, which yields a finite width for the peak in $\mathrm{Im}\,\chi(\mathbf{q},\omega)$.

B. Numerical calculation

Now we perform extensive numerical calculations of $\mathrm{Im}\,\chi(\mathbf{q},\omega)$ with a small finite $\Gamma=0.01J$ in the denominator of Eq. (17). Although the choice of a finite Γ is mainly done for numerical convenience, it also simulates damping of electrons by static defects in real materials, and broadening due to limited energy resolution in inelastic neutron scattering experiments.

This section is composed of six parts, where the first three deal with the isotropic case ($\alpha=0$) and the last three with the effects due to anisotropy ($\alpha\neq 0$). The former are intended to give a comprehensive analysis of magnetic excitations in bilayer cuprates such as YBCO, without taking effects which are specifically due to in-plane anisotropy into account: (1) $(\mathbf{q},\omega)$ maps of $\mathrm{Im}\,\chi(\mathbf{q},\omega)$ for a sequence of δ for both odd and even channels, (2) $\mathbf{q}$ maps for a sequence of ω, and (3) T dependence. The latter are dedicated to anisotropy effects on magnetic excitations and their enhancement by *d*FSD correlations: (4) $\mathbf{q}$ maps for a sequence of ω, (5) $\mathbf{q}$ maps for several choices of δ, and (6) $\mathbf{q}$ maps for a sequence of temperatures.

1. $(\mathbf{q},\omega)$ *maps for* $\alpha=0$

Figure 7 shows intensity maps of $\mathrm{Im}\,\chi(\mathbf{q},\omega)$ for a sequence of hole densities δ for the odd channel (left-hand panels) and the even channel (right-hand panels); the $\mathbf{q}$ scan direction is shown in the inset of Fig. 6. The threshold energy $\omega_{\mathrm{th}}(\mathbf{q})$ [Eq. (22)] is also plotted with a gray dotted line. Figure 7(a) shows a result in the vicinity of the AF instability. Strong intensity is seen well below $\omega_{\mathrm{th}}(\mathbf{q})$, indicating collective particle-hole excitations with the upward dispersion described by Eq. (25). This soft collective mode reflects the commensurate AF instability at $\delta\approx 0.064$. The mode disperses as a function of $\mathbf{q}$ and mixes into the particle-hole continuum at sufficiently large distance from $\mathbf{Q}$, where it becomes overdamped; it is faintly visible [due to the limited resolution of the color scale in Fig. 7(a)]. When δ is slightly increased, the soft collective mode rapidly shifts to higher energies. It has a nearly flat dispersion around $\mathbf{q}=\mathbf{Q}$ for $\delta=0.08$ [Fig. 7(b)] and a clear downward dispersion for $\delta=0.12$ [Fig. 7(c)]. In the particle-hole continuum above $\omega_{\mathrm{th}}(\mathbf{q})$, enhanced intensity is seen in Figs. 7(b) and 7(c) in a region tracing an upward dispersion. This can be interpreted as an overdamped collective excitation near $\omega_{\mathbf{Q}}^{\mathrm{res}}$, as we shall discuss later. With further increasing δ, the collective mode is pushed up to higher energy and appears only close to $\omega=\omega_{\mathrm{th}}(\mathbf{Q})$ [Fig. 7(d)]. Above $\omega_{\mathrm{th}}(\mathbf{Q})$, the spectrum broadens and the structures become less clear. For $\delta=0.20$ [Fig. 7(e)], the collective mode does not appear and we just see that the continuum spectrum has strong intensity near $\mathbf{q}=\mathbf{Q}$ and $\omega=\omega_{\mathrm{th}}(\mathbf{Q})$, and a very broad featureless distribution above. As a function of δ, Figs. 7(a)–7(e) show that the spectral weight becomes larger at lower δ (see values of the color map index) due to the proximity to the AF instability.

The corresponding results for the even channel are shown in the right-hand panels in Fig. 7. The overall features look the same as those of the odd channel. Close to the AF instability [Fig. 7(f)], however, the collective mode retains the downward dispersion and does not show softening, reflecting the fact that the AF instability is driven by the odd channel. The collective mode is pushed up to higher energy with δ [Figs. 7(g) and 7(h)] and appears inside the continuum in Fig. 7(i) in the sense that Eq. (23) is still satisfied. The mode in the continuum is substantially overdamped but has the same $|\mathbf{q}-\mathbf{Q}|^2$ dispersion as Eq. (25). The coefficient, however, is not given by Eq. (26), which is valid only if $\mathrm{Im}\,\chi_0(\mathbf{q},\omega_{\mathbf{q}}^{\mathrm{res}})=0$. Figure 7(j) looks similar to Fig. 7(i), but Eq. (23) is not satisfied any longer and the strong intensity results from individual excitations. Compared to the odd channel, we see that spectral weight of the even channel is overall suppressed and broadened. This difference comes from two effects: (i) the suppression of $|J(\mathbf{Q})|$ for the even channel near $\mathbf{q}=\mathbf{Q}$ [see Eq. (20)], and (ii) different particle-hole scattering processes, namely interband scatterings for the odd channel and the intraband scatterings for the even channel. The former (latter) effect is dominant for low (high) δ.

To see the intensity profile of $\mathrm{Im}\,\chi(\mathbf{q},\omega)$ more clearly, we replot Fig. 7(c) by separating it into three energy regions in the left-hand panel in Fig. 8 with an optimized color map scale in each; the right-hand panel is a map of $|1+J(\mathbf{q})\mathrm{Re}\,\chi_0(\mathbf{q},\omega)|$, which serves to quantify the collective character of magnetic excitations [see Eq. (23)]; the cross symbols indicate peak intensity positions of $\mathrm{Im}\,\chi(\mathbf{q},\omega)$. For $\omega \lesssim \omega_{\mathbf{Q}}^{\mathrm{res}}=0.403J$, the in-gap collective mode has a downward

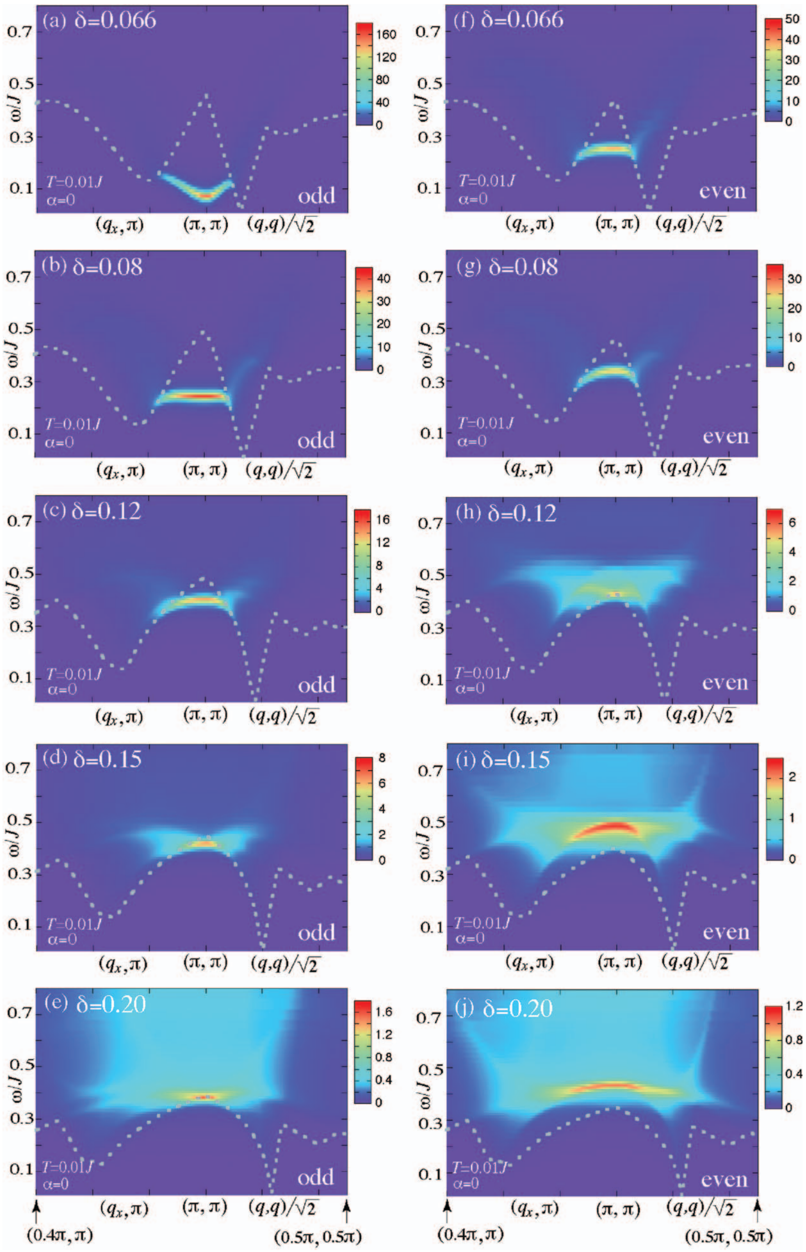

FIG. 7. (Color) $(\mathbf{q},\omega)$ maps of Im $\chi(\mathbf{q},\omega)$ for a sequence of doping concentrations δ at $T=0.01J$ and $\alpha=0$ for both odd (left-hand panels) and even (right-hand panels) channels; the gray dotted line is the threshold energy $\omega_{\mathrm{th}}(\mathbf{q})$; the $\mathbf{q}$ scan directions are shown in the inset of Fig. 6: $(0.4\pi,\pi)\leq\mathbf{q}\leq(\pi,\pi)$ and $(\pi,\pi)\geq\mathbf{q}\geq(0.5\pi,0.5\pi)$.

dispersion. This collective mode is however realized only in a limited energy region. See the region where $|1+J(\mathbf{q})\mathrm{Re}\,\chi_0(\mathbf{q},\omega)|$ becomes zero in the right-hand panel; at lower ω, $|1+J(\mathbf{q})\mathrm{Re}\,\chi_0(\mathbf{q},\omega)|$ remains finite such that the peak in Im $\chi(\mathbf{q},\omega)$ does not correspond to a genuine collective mode. With further decreasing ω the IC signals are substantially diminished, while the DIC signals continue down to zero energy. For $\omega>\omega_{\mathbf{Q}}^{\mathrm{res}}$, we see another dispersive structure inside the continuum. This upward dispersion can be interpreted as an overdamped collective excitation up to $\omega\sim0.50J$ in the sense that $|1+J(\mathbf{q})\mathrm{Re}\,\chi_0(\mathbf{q},\omega)|$ becomes zero near the peak position. Note that this overdamped mode is not directly connected with the downward collective mode below $\omega_{\mathbf{Q}}^{\mathrm{res}}$. Although the overdamped mode seems to continue smoothly up to higher energy in the left-hand panel, it changes into a peak of individual excitations as seen from the finite value of $|1+J(\mathbf{q})\mathrm{Re}\,\chi_0(\mathbf{q},\omega)|$ in the right-hand panel.

In Fig. 9, we plot Im $\chi(\mathbf{q},\omega)$ at $\mathbf{q}=\mathbf{Q}$ as a function of ω for (a) $\delta=0.08$ and 0.15, and (b) $\delta=0.20$. The sharp peak for $\delta=0.08$ corresponds to the collective mode; the continuum cannot be seen on the scale of Fig. 9(a). For $\delta=0.15$ in the odd channel, we see both the collective mode at $\omega=0.42J$ and the continuum above $\omega=0.45J$; the two are not completely separated because of finite Γ and T. The peak at $\omega=0.49J$ for the even channel is a collective mode, but its peak width is much broader than that for the odd channel, indicating a much shorter lifetime of the mode. The odd channel spectrum for $\delta=0.20$ is similar to that for $\delta=0.15$. The peak at $\omega=0.38J$, however, is not a collective mode; Eq. (23) is not satisfied any longer. Similarly the peak for the even channel results just from individual excitations.

We summarize the peak position of Im $\chi(\mathbf{q},\omega)$ at $\mathbf{q}=\mathbf{Q}$, which we refer to as $\omega=\omega_{\mathbf{Q}}$, as a function of δ in Fig. 10; $\omega_{\mathbf{Q}}$ is equivalent to $\omega_{\mathbf{Q}}^{\mathrm{res}}$ when Eq. (23) is satisfied; the lower edge energy of particle-hole continuum, $\omega_{\mathrm{th}}(\mathbf{Q})$, is also plot-

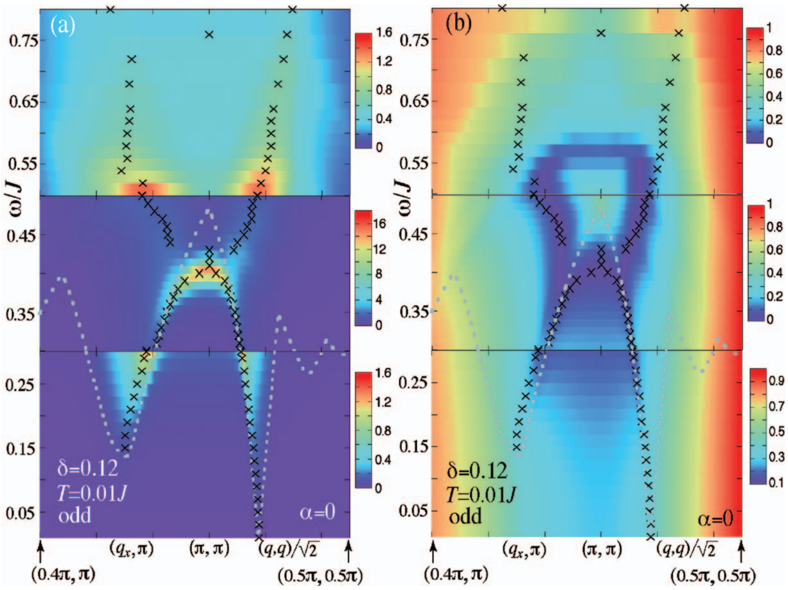

FIG. 8. (Color) $(\mathbf{q},\omega)$ maps of Im $\chi(\mathbf{q},\omega)$ (a) and $|1+J(\mathbf{q})\mathrm{Re}\,\chi_0(\mathbf{q},\omega)|$ (b) for $\delta=0.12$, $T=0.01J$, and $\alpha=0$ in the odd channel; $\mathbf{q}$-scans as in Fig. 7. The cross symbols represent the highest weight positions of Im $\chi(\mathbf{q},\omega)$ along $\mathbf{q}=(q_x,\pi)$ and $(q,q)/\sqrt{2}$, respectively.

ted by the bold gray lines; we consider the region, $\delta \geq 0.064$, below which the AF instability takes place. With increasing doping, $\omega_{\mathbf{Q}}$ increases rapidly for both channels. For the odd channel, $\omega_{\mathbf{Q}}$ has a broad maximum around $\delta=0.15$ and merges into the lower edge of particle-hole continuum; the particle-hole bound state is realized for $\delta \lesssim 0.17$ (solid circles in Fig. 10). For the even channel the bound state is realized in the same doping region as for the odd channel (solid triangles), but appears inside the continuum in $0.12 \lesssim \delta \lesssim 0.17$ accompanied by the discontinuous change of $\omega_{\mathbf{Q}}^{\mathrm{res}}$. This jump is due to the fact that the even channel consists of two different intraband scattering processes, within the bonding band and within the antibonding band.

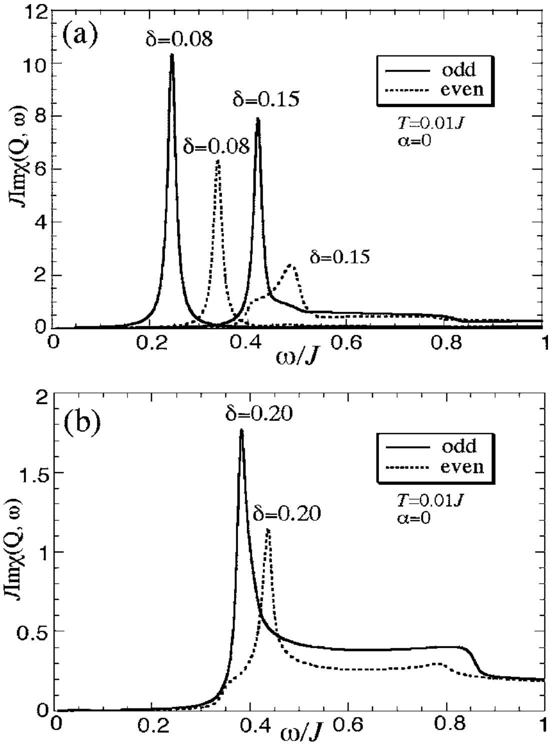

FIG. 9. ω dependence of Im $\chi(\mathbf{Q},\omega)$ for $\delta=0.08$ and 0.15 (a), and $\delta=0.20$ (b) for the odd and even channels; the results for $\delta=0.08$ are multiplied by 0.2.

2. q maps for $\alpha=0$

We next show $\mathbf{q}$ maps of Im $\chi(\mathbf{q},\omega)$ around $\mathbf{q}=\mathbf{Q}$ for a sequence of energies ω for $\delta=0.12$. At low ω [Fig. 11(a)], strong spectral weight is localized in the region around $\mathbf{q}=(\pi\pm2\pi\eta,\pi\pm2\pi\eta)$, which is due to the particle-hole excitations around the d-wave gap nodes. With increasing ω, the scattering processes with $\mathbf{q}=(\pi\pm2\pi\eta,\pi)$ and $(\pi,\pi\pm2\pi\eta)$ begin to contribute and the strong intensity region forms a diamond shape [Fig. 11(b)]. This diamond shrinks when ω increases further [Fig. 11(c)], starts being due to collective excitations [Fig. 11(d)], and is finally reduced to the collective commensurate peak at $\omega=\omega_{\mathbf{Q}}^{\mathrm{res}}=0.403J$ [Fig. 11(e)]. Above $\omega_{\mathbf{Q}}^{\mathrm{res}}$ [Fig. 11(f)], the DIC spectral weight becomes

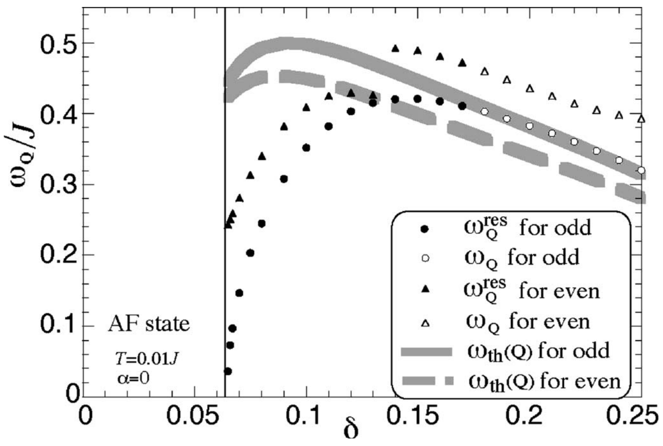

FIG. 10. Doping dependence of $\omega_{\mathbf{Q}}$ for the odd and even channels at $T=0.01J$ and $\alpha=0$; the superscript "res" indicates that Eq. (23) is satisfied at $\mathbf{q}=\mathbf{Q}$ and $\omega=\omega_{\mathbf{Q}}$; $\omega_{\mathrm{th}}(\mathbf{Q})$ is also plotted with bold gray lines for both channels.

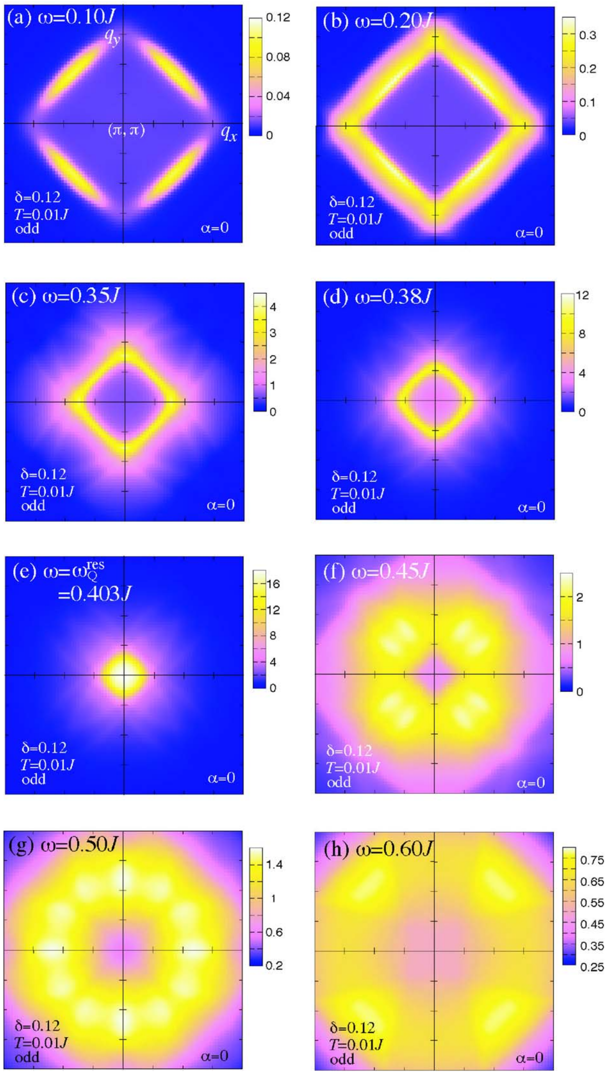

FIG. 11. (Color online) $\mathbf{q}$ maps of Im $\chi(\mathbf{q},\omega)$ for a sequence of energies ω in $0.6\pi \leq q_x, q_y \leq 1.4\pi$ for $\delta=0.12$, $T=0.01J$, and $\alpha=0$ in the odd channel.

dominant with rather broad features. While the spectral weight difference between the DIC and IC positions is not sizable and the DIC structures are smeared out in a certain energy range [Fig. 11(g)], the DIC signals seem to disperse outwards with increasing ω [Figs. 11(f)–11(h)] as expected from Fig. 8. Note that this upward dispersive feature is not a true collective mode, as discussed already in connection with Fig. 8.

The spectral weight distribution in $\mathbf{q}$-space for other doping rates, $\delta=0.08$ and 0.15, is shown in Fig. 12 for $\omega < \omega_{\mathbf{Q}}^{\rm res}$ (left-hand panels) and $\omega > \omega_{\mathbf{Q}}^{\rm res}$ (right-hand panels). For $\omega < \omega_{\mathbf{Q}}^{\rm res}$ we see that the strong weight forms a diamond shape independent of δ, and the IC signals become stronger than the DIC peaks for higher δ. For $\omega > \omega_{\mathbf{Q}}^{\rm res}$, on the other hand, the DIC structure is clearly seen at relatively low δ, while the spectral weight spreads broader with δ (see also Fig. 7).

To understand the intensity distribution in Fig. 11, we write the imaginary part of Eq. (19) as

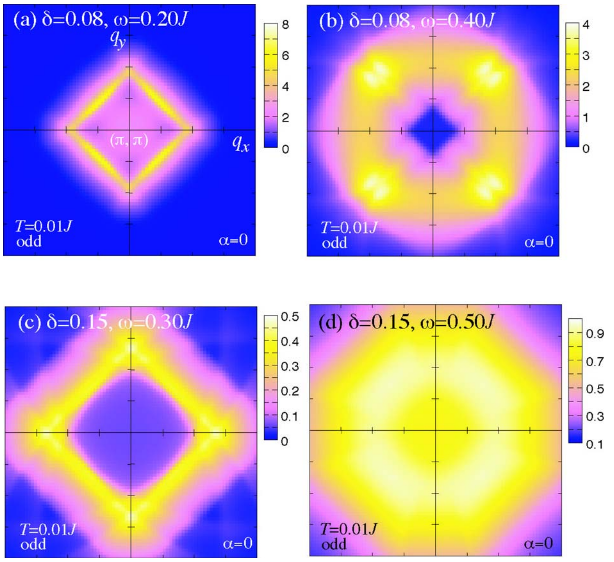

FIG. 12. (Color online) $\mathbf{q}$ maps of Im $\chi(\mathbf{q},\omega)$ in $0.6\pi \leq q_x, q_y \leq 1.4\pi$ for $\delta=0.08$ (upper panels) and 0.15 (lower panels) for $T=0.01J$, and $\alpha=0$ in the odd channel. The energy is set below (above) $\omega_{\mathbf{Q}}^{\rm res}$ in left (right) panels: $\omega_{\mathbf{Q}}^{\rm res}=0.245J$ and $0.421J$ for $\delta=0.08$ and 0.15, respectively.

$$\mathrm{Im}\,\chi(\mathbf{q},\omega) = \frac{\mathrm{Im}\,\chi_0(\mathbf{q},\omega)}{[1+J(\mathbf{q})\mathrm{Re}\,\chi_0(\mathbf{q},\omega)]^2 + [J(\mathbf{q})\mathrm{Im}\,\chi_0(\mathbf{q},\omega)]^2}. \tag{27}$$

We must consider both $|J(\mathbf{q})\mathrm{Im}\,\chi_0(\mathbf{q},\omega)|$ and $|1+J(\mathbf{q})\mathrm{Re}\,\chi_0(\mathbf{q},\omega)|$, which we show in the left-hand panel and the right-hand panel in Fig. 13, respectively, at the same ω as in Fig. 11; the structure of Im $\chi_0(\mathbf{q},\omega)$ is essentially the same as that of $J(\mathbf{q})$Im $\chi_0(\mathbf{q},\omega)$. Two typical energy scales, $\omega_{\mathbf{Q}}^{\rm res}$ and $\omega_{\rm th}(\mathbf{Q})$, characterize the spectral weight distribution of Im $\chi(\mathbf{q},\omega)$.

(1) For $\omega \ll \omega_{\mathbf{Q}}^{\rm res}$, we find $|1+J(\mathbf{q})\mathrm{Re}\,\chi_0(\mathbf{q},\omega)| \gg |J(\mathbf{q})\mathrm{Im}\,\chi_0(\mathbf{q},\omega)|$ in Figs. 13(a), 13(a′), 13(b), and 13(b′). Since the $\mathbf{q}$ dependence of Re $\chi_0(\mathbf{q},\omega)$ is weak around $\mathbf{q}=\mathbf{Q}$ we have Im $\chi(\mathbf{q},\omega) \propto$ Im $\chi_0(\mathbf{q},\omega)$, that is, the weight distribution in Figs. 11(a) and 11(b) is determined mainly by Im $\chi_0(\mathbf{q},\omega)$.

(2) For $\omega \lesssim \omega_{\mathbf{Q}}^{\rm res}$ [Figs. 13(c) and 13(c′)], the minimum values of $|1+J(\mathbf{q})\mathrm{Re}\,\chi_0(\mathbf{q},\omega)|$, become comparable with $|J(\mathbf{q})\mathrm{Im}\,\chi_0(\mathbf{q},\omega)|$ in a certain $\mathbf{q}$ region. From Eq. (27), therefore, a strong weight of Im $\chi(\mathbf{q},\omega)$ is determined by the minimum position of $|1+J(\mathbf{q})\mathrm{Re}\,\chi_0(\mathbf{q},\omega)|$, not by peak position of Im $\chi_0(\mathbf{q},\omega)$. Since Im $\chi_0(\mathbf{q},\omega)$ does not have an apparent structure in the region where $|1+J(\mathbf{q})\mathrm{Re}\,\chi_0(\mathbf{q},\omega)|$ takes minima, it depends on details which signal can be stronger, the IC or the DIC. In our model, the IC signals tend to be stronger than the DIC signals at higher δ.

(3) At $\omega \approx \omega_{\mathbf{Q}}^{\rm res}$, $|1+J(\mathbf{q})\mathrm{Re}\,\chi_0(\mathbf{q},\omega)|$ can vanish for suitable $\mathbf{q}$ vectors [Figs. 13(d′) and 13(e′)], leading to Im $\chi(\mathbf{q},\omega) \propto$ Im $\chi_0(\mathbf{q},\omega)^{-1}$. Since Im $\chi_0(\mathbf{q},\omega)$ also can become very small in the same $\mathbf{q}$ region [Figs. 13(d) and 13(e)], the strongest weight of Im $\chi(\mathbf{q},\omega)$ appears there, corresponding to a collective mode.

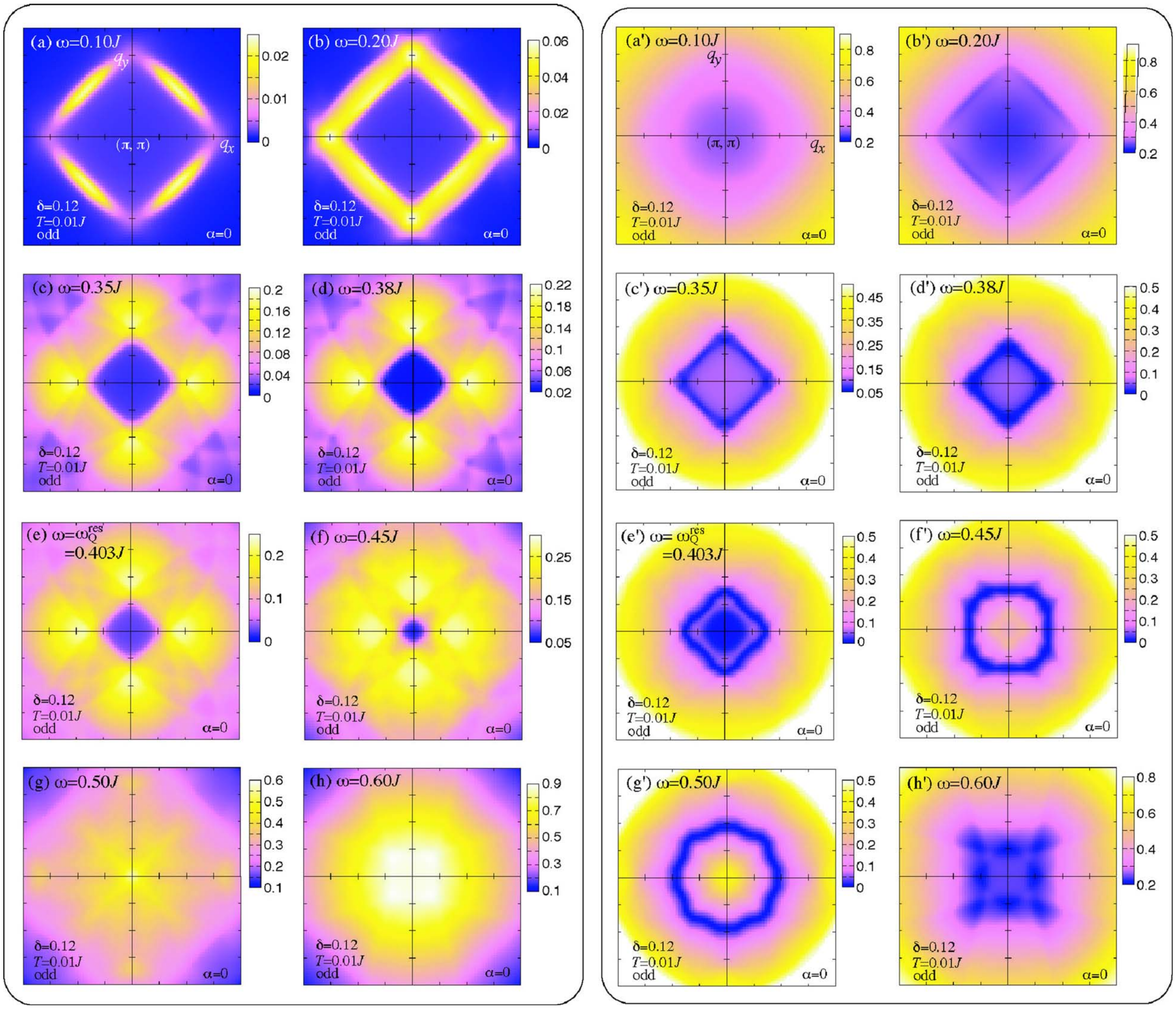

FIG. 13. (Color online) $\mathbf{q}$ maps of $|J(\mathbf{q})\mathrm{Im}\,\chi_0(\mathbf{q},\omega)|$ (left panel) and $|1+J(\mathbf{q})\mathrm{Re}\,\chi_0(\mathbf{q},\omega)|$ (right panel) for a sequence of energies ω in $0.6\pi \leq q_x, q_y \leq 1.4\pi$ for $\delta=0.12$, $T=0.01J$, and $\alpha=0$ in the odd channel. In (c′)–(g′), the maps are restricted to $\mathbf{q}$ with $|1+J(\mathbf{q})\mathrm{Re}\,\chi_0(\mathbf{q},\omega)| \leq 0.5$ to get a better contrast in the interesting region.

(4) For $\omega_{\mathbf{Q}}^{\mathrm{res}} \lesssim \omega \lesssim \omega_{\mathrm{th}}(\mathbf{Q})$, $|1+J(\mathbf{q})\mathrm{Re}\,\chi_0(\mathbf{q},\omega)|$ vanishes in the region where $\mathrm{Im}\,\chi_0(\mathbf{q},\omega)$ has IC peaks [Figs. 13 (f′)]. Since $\mathrm{Im}\,\chi(\mathbf{q},\omega) \propto \mathrm{Im}\,\chi_0(\mathbf{q},\omega)^{-1}$ when $1+J(\mathbf{q})\mathrm{Re}\,\chi_0(\mathbf{q},\omega)=0$, the IC spectral weight is substantially diminished and $\mathrm{Im}\,\chi(\mathbf{q},\omega)$ shows DIC peaks as seen in Fig. 11(f).

(5) At $\omega \approx \omega_{\mathrm{th}}(\mathbf{Q})$, the IC peaks of $|J(\mathbf{q})\mathrm{Im}\,\chi_0(\mathbf{q},\omega)|$ merge into a commensurate peak as shown in Fig. 13(g). $|J(\mathbf{q})\mathrm{Im}\,\chi_0(\mathbf{q},\omega)|$ does not have an apparent structure around the region where $|1+J(\mathbf{q})\mathrm{Re}\,\chi_0(\mathbf{q},\omega)|$ vanishes [Fig. 13(g′)]. Hence the strong weight of $\mathrm{Im}\,\chi(\mathbf{q},\omega)$ has a similar distribution to that of $1+J(\mathbf{q})\mathrm{Re}\,\chi_0(\mathbf{q},\omega) \approx 0$, and shows a “ring” in Fig. 11(g).

(6) For $\omega \gtrsim \omega_{\mathrm{th}}(\mathbf{Q})$, $\mathrm{Im}\,\chi(\mathbf{q},\omega)$ has strongest intensity in the region where $|1+J(\mathbf{q})\mathrm{Re}\,\chi_0(\mathbf{q},\omega)| \approx |J(\mathbf{q})\mathrm{Im}\,\chi_0(\mathbf{q},\omega)|$ [compare Fig. 11(h) with Figs. 13(h) and 13(h′)].

The spectral distribution of Figs. 12(a)–12(d) corresponds to the cases (2), (4), (2), and (6), respectively.

3. T dependence for $\alpha=0$

So far we have presented results for a fixed temperature $T=0.01J$. Now we discuss the T dependence of $\mathrm{Im}\,\chi(\mathbf{q},\omega)$. In Fig. 14, we plot $\mathrm{Im}\,\chi(\mathbf{q},\omega)$ at $\mathbf{q}=\mathbf{Q}$ as a function of ω for several choices of T for $\delta=0.10$ in the odd channel. The d-wave gap disappears at $T_{\mathrm{RVB}}=0.139J$ for this doping. We see that the sharp peak of $\mathrm{Im}\,\chi(\mathbf{Q},\omega)$ survives as long as the d-wave gap exists. The peak energy is determined mainly by minimizing $|1+J(\mathbf{Q})\mathrm{Re}\,\chi_0(\mathbf{Q},\omega)|$. The T dependence of the peak energy is shown in the inset of Fig. 14; it follows approximately the T dependence of the d-wave gap [see Fig. 2(a)]. With increasing T low-energy spectral weight proportional to ω becomes noticeable, and $\mathrm{Im}\,\chi(\mathbf{Q},\omega)$ evolves smoothly toward the spectrum in the normal state ($T > T_{\mathrm{RVB}}$), where the sharp peak at finite ω disappears.

The temperature dependence of $\mathbf{q}$ maps is shown in Fig. 15 for several choices of T at $\delta=0.10$ and $\omega=0.25J$. Strong

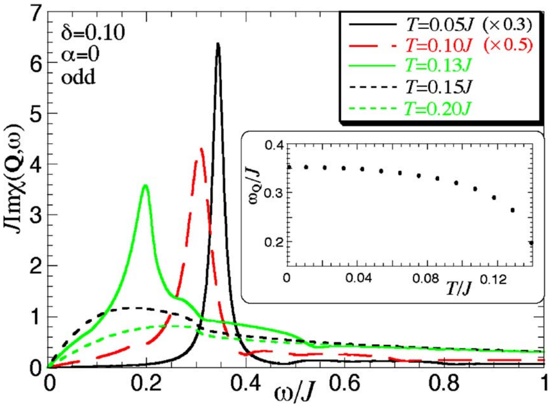

FIG. 14. (Color online) ω dependence of Im $\chi(\mathbf{Q},\omega)$ for several choices of T for δ=0.10, and α=0 in the odd channel; here T_{RVB} =0.139J; for T=0.05J and 0.10J, Im $\chi(\mathbf{Q},\omega)$ is multiplied by 0.3 and 0.5, respectively. The inset shows the T dependence of the peak energy of Im $\chi(\mathbf{Q},\omega)$.

intensity of Im $\chi(\mathbf{q},\omega)$ forms a diamond shape at low T. Although the diamond shape is retained with increasing T, the weight inside the diamond becomes stronger, leading to a dominant commensurate signal above $T\sim 0.11J$. The commensurate signal thus dominates already at temperatures slightly below the onset temperature of d-wave singlet pairing T_{RVB}=0.139J.

A $(\mathbf{q},\omega)$ map of Im $\chi(\mathbf{q},\omega)$ is shown in Fig. 16(a) for T =0.12J ($<T_{\mathrm{RVB}}$), where the energy region is separated into three with different color scales; the cross symbols mark highest weight positions along $\mathbf{q}=(q_x,\pi)$ and $(q,q)/\sqrt{2}$. The strongest weight appears at $\mathbf{q}=\mathbf{Q}$ and $\omega\approx 0.26J$. Below this energy IC structures are not realized any longer and the spectrum shows a broad commensurate structure. However, in the high energy region ($\omega \gtrsim 0.30J$) DIC signals still survive as well as IC signals. When T is further increased above T_{RVB} [Fig. 16(b)], neither IC nor DIC structures are realized. The strong intensity is centered around $\mathbf{q}=\mathbf{Q}$ and broadly spreads out. The right-hand panels in Fig. 16 are corresponding results for the even channel. Overall features look similar as for the odd channel except that the spectral weight becomes rather broadened. Although the peak positions form a rather complex pattern in Fig. 16(c), an upward dispersion for $0.3J \lesssim \omega \lesssim 0.45J$ can still be recognized together with a remnant of the downward dispersion for $0.2J \lesssim \omega \lesssim 0.25J$.

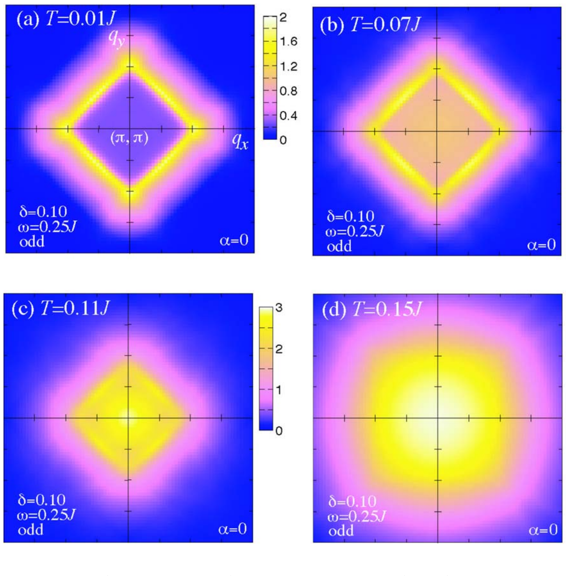

FIG. 15. (Color online) $\mathbf{q}$ maps of Im $\chi(\mathbf{q},\omega)$ for a sequence of temperatures in $0.6\pi \le q_x, q_y \le 1.4\pi$ for δ=0.10, ω=0.25J, and α =0 in the odd channel; here T_{RVB}=0.139J.

4. ω dependence of q *maps for α≠0*

In the following three subsections, we present results for Im $\chi(\mathbf{q},\omega)$ for α=−0.05 to discuss effects due to an in-plane anisotropy and their enhancement by dFSD correlations.

Figure 17 shows $\mathbf{q}$ maps of Im $\chi(\mathbf{q},\omega)$ for a sequence of energies ω for δ=0.12 and T=0.01J; the corresponding results for α=0 were shown in Fig. 11. At low ω, the DIC signals appear, and form a high intensity region which is a bit distorted compared to Fig. 11(a), due to the in-plane anisotropy. These DIC signals come from nodal scatterings. Note that the nodes of the singlet pairing deviate slightly from the diagonal direction because of $\Delta_x \neq \Delta_y$ and finite Δ_z in Eqs. (5) and (6). Figures 17(b)–17(d) are results for larger $\omega<\omega_{\mathbf{Q}}^{\mathrm{res}}$. Appreciable weight appears on both the q_x and q_y axes and in this sense a nearly two-dimensional excitation spectrum is obtained even if the antibonding FS becomes open as in Fig. 4. Analogous behavior was already found for the single layer t-J model in Ref. 45. Effects of the anisotropy are seen in (i) the difference of the IC peak positions, namely $(\pi\pm 2\pi\eta_x,\pi)$ and $(\pi,\pi\pm 2\pi\eta_y)$ with $\eta_x\neq\eta_y$, leading to a deformed diamond shape, and (ii) the relative peak intensity difference of the two IC peaks. The latter however depends strongly on ω and δ even if α is fixed. For example, the IC peak at $\mathbf{q}=(\pi,\pi\pm 2\pi\eta_y)$ is a bit higher than that at $\mathbf{q}=(\pi\pm 2\pi\eta_x,\pi)$ at ω=0.20J [Fig. 17(b)], while the order is reversed at ω=0.35J [Fig. 17(c)]. Moreover, as we shall discuss in Sec. V B, the peak intensity difference can depend strongly on details of the band structures and thus on models. On the other hand, the former is a robust feature of Im $\chi(\mathbf{q},\omega)$. When the difference of the IC peak position, $\Delta\eta=\eta_x-\eta_y$, is taken as a measure of the anisotropy of the IC peaks, we have $\Delta\eta>0$ for $\alpha<0$ and in addition $\Delta\eta\propto\alpha$ in good approximation at least up to $|\alpha|\sim 0.1$. Furthermore, the ω dependence of $\Delta\eta$ is weak. In Fig. 18 we plot η_x and η_y as a function of ω. While η_x and η_y depend on ω, one finds $\Delta\eta>0$ for all $\omega<\omega_{\mathbf{Q}}^{\mathrm{res}}$, and a weak ω dependence of $\Delta\eta$ except for the region of $\omega\approx\omega_{\mathbf{Q}}^{\mathrm{res}}$ where both η_x and η_y tend to zero.

Figure 17(e) corresponds to the energy $\omega=\omega_{\mathbf{Q}}^{\mathrm{res}}$. While the strongest weight appears at $\mathbf{q}=\mathbf{Q}$ for that energy, Im $\chi(\mathbf{q},\omega_{\mathbf{Q}}^{\mathrm{res}})$ has an apparent elliptic distribution in the $\mathbf{q}$ plane. Figures 17(f)–17(h) are for $\omega>\omega_{\mathbf{Q}}^{\mathrm{res}}$. In Fig. 17(f), the strongest weight appears along the diagonal direction, which is a remnant of the DIC signal for α=0 (Fig. 11). The strong weight distribution, however, forms a rectangular shape and shows a pronounced anisotropy. As energy is increased a little, Im $\chi(\mathbf{q},\omega)$ shows one-dimensional-like signatures in Fig. 17(g) even with a small anisotropy (5%). To understand this one-dimensional pattern, we go back to Figs. 13(g) and

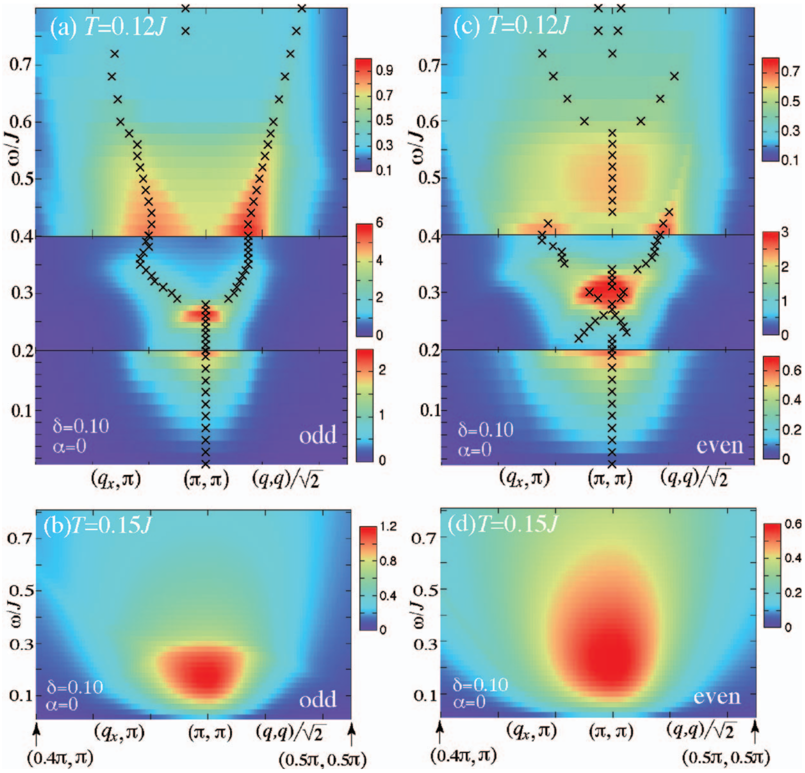

FIG. 16. (Color) $(\mathbf{q},\omega)$ maps of Im $\chi(\mathbf{q},\omega)$ at $T<T_{\mathrm{RVB}}=0.139J$ (a) and (c), and $T>T_{\mathrm{RVB}}$ (b) and (d) for $\delta=0.10$ and $\alpha=0$; the left-hand (right-hand) panels are for the odd (even) channel; $\mathbf{q}$-scans as in Fig. 7. The cross symbols in (a) and (c) represent the highest weight positions along $\mathbf{q}=(q_x,\pi)$ and $(q,q)/\sqrt{2}$.

13(g'). For $\alpha=-0.05$, Im $\chi_0(\mathbf{q},\omega)$ still shows a commensurate signal but the spectral weight spreads out largely along the q_x direction. Since $|1+J(\mathbf{q})\mathrm{Re}\,\chi_0(\mathbf{q},\omega)|$ vanishes around $\mathbf{q}=\mathbf{Q}$ as shown in Fig. 13(g'), the resulting Im $\chi(\mathbf{q},\omega)$ shows enhanced spectral weight along the q_y direction, leading to Fig. 17(g). With further increasing ω, however, the spectral weight becomes much broader [Fig. 17(h)] and the anisotropy becomes less apparent. For $\omega>\omega_{\mathbf{Q}}^{\mathrm{res}}$ therefore the spectral weight distribution forms various patterns and is very sensitive to energy. This is in sharp contrast to the robust feature of the deformed diamond shape distribution for $\omega<\omega_{\mathbf{Q}}^{\mathrm{res}}$, which enables us to define $\Delta\eta$ as a measure of the anisotropy of the magnetic excitations.

5. δ dependence of q maps for $\alpha\neq 0$

The left-hand panels of Fig. 19 show $\mathbf{q}$ maps of Im $\chi(\mathbf{q},\omega)$ for a sequence of doping concentrations δ; the energy ω is below $\omega_{\mathbf{Q}}^{\mathrm{res}}$ (actually below $\omega_{\mathbf{Q}}$ for $\delta=0.20$, where no collective mode exists, see Fig. 10). Appreciable intensity appears along a deformed diamond for all δ. Although the renormalized band anisotropy decreases with increasing δ [Fig. 3(b)], the anisotropy of Im $\chi(\mathbf{q},\omega)$ is enhanced. To identify the influence of dFSD correlations, we compare these results with the corresponding results for the bare anisotropy on the right-hand panels of Fig. 19. The latter are calculated by switching off the dFSD correlations, that is, we impose the same bare anisotropy $\alpha=-0.05$, but use mean fields for $\alpha=0$. We see that the effect of the bare anisotropy on Im $\chi(\mathbf{q},\omega)$ is doping dependent even for fixed (doping-independent) α and becomes less pronounced at lower δ. In particular, the diamond is almost symmetric for $\delta=0.08$ and 0.12 [Figs. 19(a′) and 19(b′)]. That is, the dFSD correlations are particularly important to understand the anisotropy of Im $\chi(\mathbf{q},\omega)$ at lower δ [Figs. 19(a) and 19(b)]. This holds for both odd and even channels and similar results are obtained for the even channel.

6. T dependence of q maps for $\alpha\neq 0$

Momentum space maps of Im $\chi(\mathbf{q},\omega)$ for a sequence of temperatures are shown in the left-hand panel of Fig. 20 for $\delta=0.10$ and $\omega=0.25J$. The deformed diamond shaped distribution is rather robust against T [Figs. 20(a) and 20(b)], although the spectral weight inside the diamond gradually increases with T, as we have seen in Fig. 15. At temperatures slightly below $T_{\mathrm{RVB}}=0.133J$, the commensurate signal becomes dominant [Fig. 20(c)] and a pronounced anisotropy appears in Fig. 20(d). When T increases further, the anisotropy is however reduced [Figs. 20(e) and 20(f)]. The temperature dependence of the anisotropy in Fig. 20 is not monotonically linked to the T dependence of the band anisotropy. As seen in Fig. 3(b) for $\delta=0.10$, the band anisotropy at $T=0.13J$ is larger than that at $T=0.12J$, but does not lead to a stronger anisotropy of Im $\chi(\mathbf{q},\omega)$ at $T=0.13J$.

To analyze the relevance of dFSD correlations, we calculate Im $\chi(\mathbf{q},\omega)$ also for isotropic mean fields and show the results in the right-hand panel of Fig. 20. We see that while dFSD correlations contribute to the enhancement of the anisotropy of Im $\chi(\mathbf{q},\omega)$ at any T, such an effect becomes most pronounced at relatively high T as seen in Figs. 20(d) and 20(d′). While Fig. 20 has been obtained for fixed ω and δ, results for other parameter sets including the even channel show that the dFSD correlations typically drive a pronounced anisotropy at relatively high T ($\sim T_{\mathrm{RVB}}$).

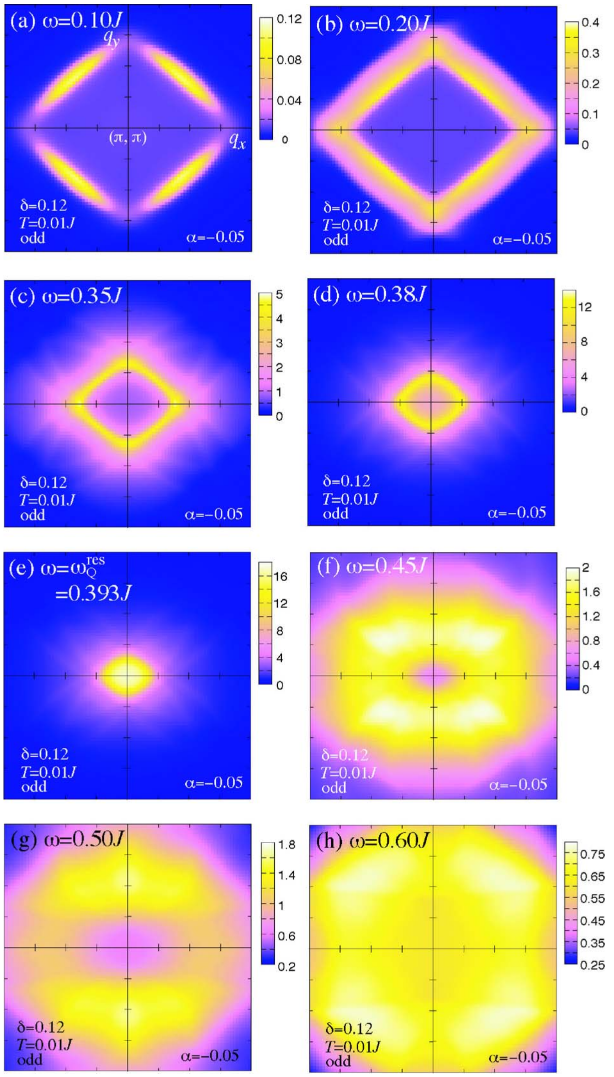

FIG. 17. (Color online) **q** maps of Im $\chi(\mathbf{q},\omega)$ for a sequence of ω in $0.6\pi \leq q_x, q_y \leq 1.4\pi$ for $\delta=0.12$, $T=0.01J$, and $\alpha=-0.05$ in the odd channel.

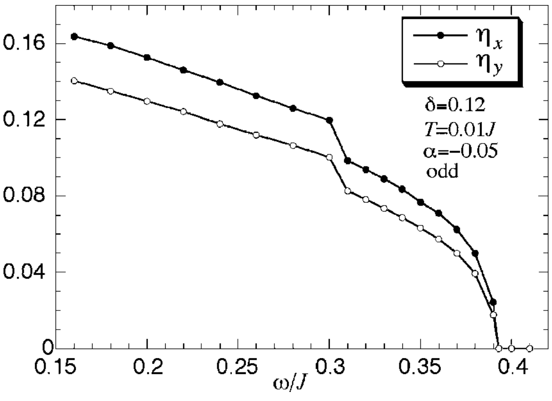

FIG. 18. Energy dependence of η_x and η_y for $\delta=0.12$, $T=0.01J$, and $\alpha=-0.05$ in the odd channel. The jump of η_x and η_y at $\omega \approx 0.3J$ is due to fine peak structures of Im $\chi(\mathbf{q},\omega)$.

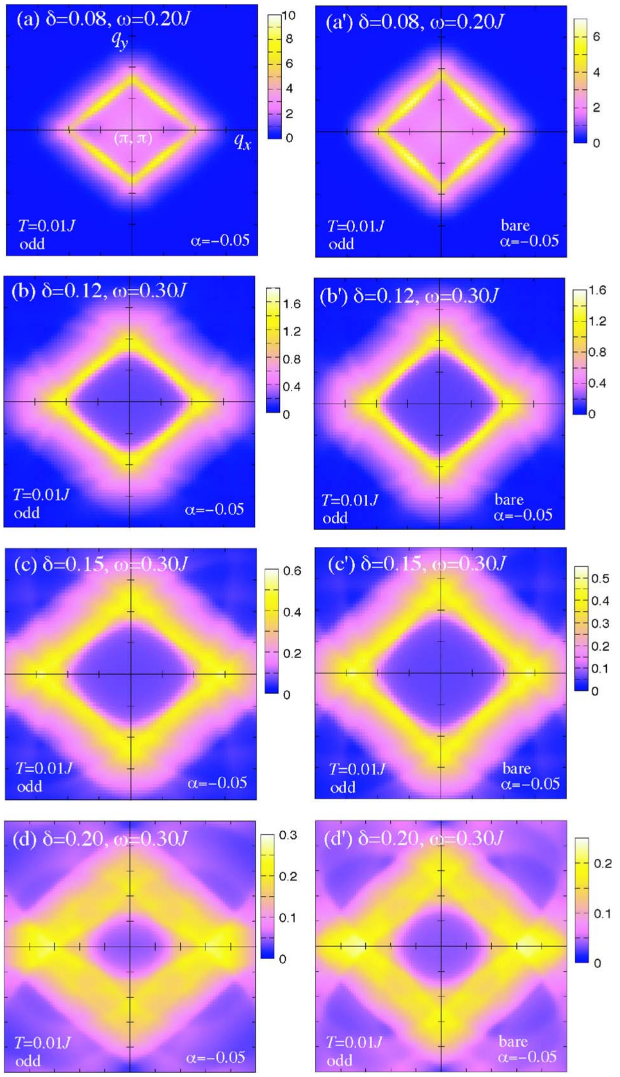

FIG. 19. (Color online) **q** maps of Im $\chi(\mathbf{q},\omega)$ for a sequence of doping concentrations δ for $T=0.01J$, and $\alpha=-0.05$ in the odd channel; ω is chosen below $\omega_{\mathbf{Q}}^{\mathrm{res}}$; the right-hand panels show the results obtained from the bare anisotropy without the enhancement due to *d*FSD correlations; **q** is scanned in $0.6\pi \leq q_x, q_y \leq 1.4\pi$ except for the panels for $\delta=0.20$ where $0.5\pi \leq q_x, q_y \leq 1.5\pi$ is taken.

V. DISCUSSION

We have investigated Im $\chi(\mathbf{q},\omega)$ in the slave-boson mean-field scheme for the bilayer *t-J* model. We summarize our results through a comparison with inelastic neutron scattering data for YBCO. Experimental data are well summarized in Refs. 1, 12, 79, and 84. It should be kept in mind that in the slave-boson mean-field theory[43] T_{RVB} must be interpreted as pseudogap crossover temperature T^* in the underdoped regime, and as superconducting phase transition temperature T_c in the overdoped regime of high-T_c cuprates.

A. Prominent features of magnetic excitations in YBCO

One of the most prominent features of magnetic excitations in YBCO is that IC peaks appear only below T_c or T^*,[6,10–13] which is in sharp contrast to LSCO where IC peaks

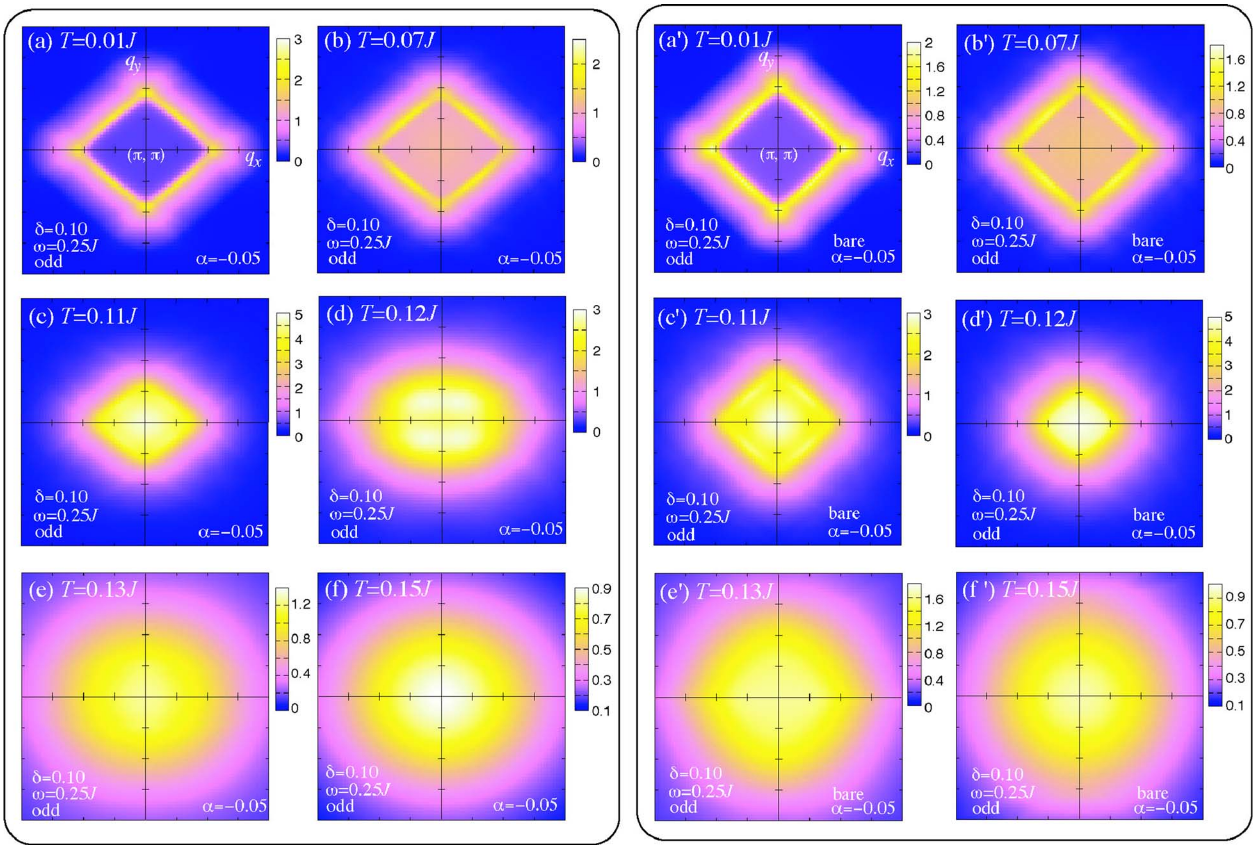

FIG. 20. (Color online) Left-hand panel: **q** maps of Im $\chi(\mathbf{q},\omega)$ for a sequence of T in $0.6\pi \leq q_x, q_y \leq 1.4\pi$ for $\delta=0.10$, $\omega=0.25J$, and $\alpha=-0.05$ in the odd channel; here $T_{\text{RVB}}=0.133J$. Right-hand panel: corresponding results for the bare anisotropy, that is, without dFSD correlations; $T_{\text{RVB}}=0.139J$ in that case.

were reported even at room temperature.[2,14] This is captured by the present theory. As shown in Fig. 15, the IC signals are obtained only at low T and change into a broad commensurate signal above $T \sim T_{\text{RVB}}$. It was pointed out a few years ago that the distinct behavior of LSCO is also captured by the present theoretical framework with different band parameters.[44,45]

Another central issue in YBCO is the so-called resonance peak, which was reported as a sharp magnetic signal at $\mathbf{q}=\mathbf{Q}$ and finite ω.[1,15–20] There are several alternative scenarios for this resonance peak.[60,107–111] In the present theory, in accordance with previous work,[28,34–40,56–58,103–106,112–114] the resonance is interpreted as a particle-hole bound state (Figs. 6 and 7). While the resonance is particularly pronounced at low T ($\ll T_{\text{RVB}}$), it starts to develop below T_{RVB} (Fig. 14), that is, below T^* in the underdoped regime and below T_c in the overdoped regime. This is consistent with experiments for optimally doped YBCO[11,15–18] and $\text{YBa}_2\text{Cu}_3\text{O}_{6.6}$.[83] The δ dependence of $\omega_{\mathbf{Q}}^{\text{res}}$ (Fig. 10) roughly agrees with experiments for both odd[12,13,81,84] and even[22,80,81] channels if we set $J \approx 100$ meV.[79] Although this agreement is based on tuning one of the band parameters, namely t/J, it is remarkable that the δ dependence of $\omega_{\mathbf{Q}}^{\text{res}}$ is reproduced within the present simple framework. We note that no genuine resonance was obtained for $\delta \gtrsim 0.18$ in Fig. 10, which however depends on the choice of Γ.

As seen from Figs. 7 and 8, the collective mode usually has a downward dispersion and is necessarily accompanied by IC signals for $\omega < \omega_{\mathbf{Q}}^{\text{res}}$. This downward dispersion was actually observed.[10,11,21,22] The resonance at $\mathbf{q}=\mathbf{Q}$ and the IC peaks observed in experiments are therefore understood as coming from the same origin. The resonance mode, however, is realized only in a limited energy region in the presence of finite damping and temperature, and loses its collective nature when it touches the continuum spectrum (Fig. 7).

The IC peaks are well-defined along the cut with $\mathbf{q}=(q_x,\pi)$ or (π,q_y) for $\omega \lesssim \omega_{\mathbf{Q}}^{\text{res}}$. In the $\mathbf{q}$ plane, however, strong intensity weight appears on a diamond shaped region as we have seen in Figs. 11(b)–11(d). Hence, the DIC peaks are also well defined along a cut with $\mathbf{q}=(q,q)/\sqrt{2}$. Although the possibility of DIC peaks was not discussed in the experimental literature, this diamond-shaped distribution was actually observed.[9] For $\omega \ll \omega_{\mathbf{Q}}^{\text{res}}$ the DIC signals become dominant [Fig. 11(a)], which is a robust feature coming from the d-wave gap nodes. These DIC signals were already predicted about a decade ago,[27,115] but have not been detected in experiments.

For $\omega > \omega_{\mathbf{Q}}^{\text{res}}$, we have obtained an upward dispersion in Figs. 7 and 8 especially at relatively low δ and have interpreted it as an overdamped collective excitation; note that this mode is not directly connected with the downward collective mode in $\omega < \omega_{\mathbf{Q}}^{\text{res}}$. An upward dispersion of DIC peaks for $\omega > \omega_{\mathbf{Q}}^{\text{res}}$ can be read off also from Figs. 11 and 12. These DIC peaks are robust at least for $\omega_{\mathbf{Q}}^{\text{res}} \lesssim \omega \lesssim \omega_{\text{th}}(\mathbf{Q})$ as discussed in Figs. 13(f) and 13(f′), although they seem to continue up to higher ω than $\omega_{\text{th}}(\mathbf{Q})$ in Figs. 7 and 8. An upward DIC dispersion was recently reported in neutron scattering experiments.[21–23]

The upward dispersing signal was associated with a genuine collective mode in Ref. 22. That interpretation was supported by a recent RPA calculation by Eremin *et al.*[106] They obtained a new resonant mode in a narrow range of incommensurate wave vectors with energies well above $\omega_{\mathbf{Q}}^{\text{res}}$. In principle, this mode exists also in our slave-boson based RPA theory. However, it depends strongly on band structure details and is very easily suppressed by temperature and damping. For our choice of parameters this mode is not apparent in the numerical results.

As seen in Figs. 16(a) and 16(c), the upward dispersion in the high energy region is rather robust to temperature while in the low energy region temperature spoils the incommensurate structures in favor of a broad commensurate signal. This behavior was detected in the most recent neutron scattering experiments.[55]

The even channel behaves qualitatively similarly to the odd channel as seen from Fig. 7. The main differences are that its intensity is overall suppressed and it has a larger energy scale (characterized by $\omega_{\mathbf{Q}}$, see also Fig. 10). These features of the even channel were actually reported in neutron scattering experiments.[22,80–85] The experiments, however, indicate a much stronger suppression of the even channel than that obtained in our calculation, especially in the low ω region. In fact, Fong *et al.*[84] concluded that the even channel was fully gaped even at $T=200$ K. Although the even channel could be suppressed more by taking a larger value of J_z in Eq. (20), such a "gap" feature is not captured by the present theory.

While the present theory captures prominent features of magnetic excitations in YBCO, the line shapes of $\text{Im}\,\chi(\mathbf{Q},\omega)$ in Fig. 9 are different from experimental data.[16,79,84] The experimentally observed peak structure, which is interpreted as resonance, is much broader. From the experimental viewpoint it is not evident that the resonance is really situated below the continuum, although we have interpreted it as an in-gap collective mode especially for the odd channel (Fig. 10). Several experimentalists[12,16,84] extract the gap from the low-energy tail of the resonance, such that the gap becomes smaller than the resonance energy by definition. From the present theoretical viewpoint, however, the gap should be defined from the lower edge of the continuum.

B. Anisotropy of magnetic excitations

Hinkov *et al.*[54] presented a clear $\mathbf{q}$ map of magnetic spectral intensity for untwinned $\text{YBa}_2\text{Cu}_3\text{O}_{6.85}$, which showed that the peak intensity at $\mathbf{q}=(\pi\pm 2\pi\eta_x,\pi)$ is larger than that at $\mathbf{q}=(\pi,\pi\pm 2\pi\eta_y)$. This map was obtained by fitting the experimental data to putative δ-peaks in $\mathbf{q}$ space smeared by a spectrometer resolution function.[116] In the present model (see Fig. 19), the peak intensity difference for $\omega<\omega_{\mathbf{Q}}^{\text{res}}$ is less sizable below $\delta\sim 0.15$ than the difference extracted from the fit to the experimental data. Hinkov *et al.*[54] also reported that the $\mathbf{q}$-integrated spectral weight difference between along $\mathbf{q}=(\pi\pm 2\pi\eta_x,\pi)$ and $\mathbf{q}=(\pi,\pi\pm 2\pi\eta_y)$ became apparently larger with decreasing ω below the resonance energy. This feature is not manifest in our results shown in Figs. 17(c)–17(e).

These discrepancies may result from details of the band structure. LDA calculations suggest[98] that seemingly small effects, such as long-range hopping integrals beyond third neighbors and the buckling of oxygen atoms, may affect the dispersion near the Fermi level without necessarily leading to strong shifts of the Fermi surface. The recently observed kink structure of the band dispersion near the Fermi level[117] should also be taken into account. The influence of band structure features on the IC peak intensity difference follows also from theoretical studies. Zhou and Li[58] showed that the direct coupling to the chain band contributes strongly to the peak intensity difference. Two recent phenomenological calculations with different band parameters also revealed the sensitivity to band structure details: in one case 22% band anisotropy[59] was required to account for the peak intensity difference reported by Hinkov *et al.*,[54] in the other only 6%.[56] There may also be ambiguities in the analysis of the experimental data, since the anisotropy of the IC peaks was deduced after a background correction, and the larger anisotropy was reported when the background became dominant, that is when the magnetic signals became very weak. If there is a magnetic signal hidden in the background, one might overestimate the IC peak intensity difference.

Since the anisotropy of the IC peak intensity is sensitive to details of the model and to ambiguities in the experimental data analysis, it seems advantageous to consider the anisotropy of the incommensurability, $\Delta\eta=\eta_x-\eta_y$, as a more robust measure of the anisotropy of $\text{Im}\,\chi(\mathbf{q},\omega)$ at low T for $\omega<\omega_{\mathbf{Q}}^{\text{res}}$. We have consistently obtained $\Delta\eta \gtreqless 0$ for $\alpha \lesseqgtr 0$ for all studied parameter sets, and moreover $\Delta\eta$ turns out to be proportional to α in good approximation at least up to $|\alpha|\sim 0.1$ without appreciable ω dependence except near $\omega_{\mathbf{Q}}^{\text{res}}$ (Fig. 18). Our result, $\Delta\eta\approx 0.02-0.03$ for $\alpha=-0.05$ (Fig. 18), is comparable with experimental data for $\text{YBa}_2\text{Cu}_3\text{O}_{6.6}$ and not inconsistent with the data for $\text{YBa}_2\text{Cu}_3\text{O}_{6.85}$ also.[54,116]

The negative sign of α corresponds to $t_x<t_y$, that is, the opposite of what one would expect from the in-plane lattice constant difference. In agreement with LDA band calculations,[87] this implies that the chains are crucial to the in-plane anisotropy in YBCO and thus to the understanding of the anisotropy of $\text{Im}\,\chi(\mathbf{q},\omega)$. The importance of chain effects was already discussed by Zhou and Li[58] in a different context. They analyzed direct coupling between CuO chains and CuO_2 planes. Such a direct coupling, however, should be small enough to ensure that $\text{Im}\,\chi(\mathbf{q},\omega)$ is well characterized by a bilayer model to be consistent with the observed q_z modulation.[7,13,15,17–19,79–81] We have therefore interpreted chain effects as mainly renormalizing the in-plane band anisotropy. We note that an LDA calculation[87] predicts that chain effects are not important to the anisotropy of t in the double chain compound $\text{YBa}_2\text{Cu}_4\text{O}_8$, for which we thus expect $t_x>t_y$. Our theory then predicts $\Delta\eta=\eta_x-\eta_y<0$ for $\omega<\omega_{\mathbf{Q}}^{\text{res}}$ at low T.

For $\omega>\omega_{\mathbf{Q}}^{\text{res}}$ we have found a pronounced spectral weight anisotropy, which however strongly depends on ω [Figs. 17(f)–17(h)]. Stock *et al.*[85] performed high energy neutron scattering experiments for partially untwinned $\text{YBa}_2\text{Cu}_3\text{O}_{6.5}$

and obtained **q** maps of the spectral weight. They reported nearly isotropic spectral weight distribution. However, their data were integrated over intervals ±7.5 meV along the energy axis, which may smear out the predicted anisotropy in Figs. 17(f)–17(h). In addition, anisotropies may be underestimated if the untwinning of the crystal is not complete. On the other hand, Hinkov *et al.*[55] observed an anisotropy of IC peaks at several choices of energy for $\omega > \omega_{\mathbf{Q}}^{\mathrm{res}}$ in almost fully untwinned $\mathrm{YBa_2Cu_3O_{6.6}}$, while full **q** maps have not yet been obtained. Further neutron scattering data for $\omega > \omega_{\mathbf{Q}}^{\mathrm{res}}$ would be useful.

At relatively high T we have found an enhanced anisotropy of $\mathrm{Im}\,\chi(\mathbf{q},\,\omega)$ [Figs. 20(c) and 20(d)]. This anisotropy is characterized by the difference of the broad commensurate peak width between the q_x direction and the q_y direction. This anisotropic peak width was actually observed in the most recent experiment for $\mathrm{YBa_2Cu_3O_{6.6}}$ in the pseudogap regime.[55]

C. Relevance of *d*FSD correlations

A sizable anisotropy of $\mathrm{Im}\,\chi(\mathbf{q},\omega)$ was reported for underdoped materials, $\mathrm{YBa_2Cu_3O_{6.5}}$ (Ref. 13) and $\mathrm{YBa_2Cu_3O_{6.6}}$.[54,55] To understand this behavior, the bare band anisotropy, without an enhancement due to *d*FSD correlations, is not sufficient. The magnetic anisotropy due to the bare band structure anisotropy decreases at lower δ for fixed α, as seen in the right-hand panels of Fig. 19. One cannot expect a larger α at lower δ since the crystal structure changes from orthorhombic to tetragonal for $y \lesssim 6.4$, and is accompanied by the disappearance of the CuO chains.[90] On the other hand, the presence of *d*FSD correlations provides a natural explanation for the observed anisotropy at low δ; the correlation effects can yield an enhanced anisotropy of magnetic excitations at low δ (Fig. 19). While we have treated *d*FSD correlations in the slave-boson mean-field approximation to the *t*-*J* model, they were shown to be present also in a recent exact diagonalization study.[67] The anisotropy of $\mathrm{Im}\,\chi(\mathbf{q},\omega)$ in optimally doped $\mathrm{YBa_2Cu_3O_{6.85}}$,[54] on the other hand, can be understood qualitatively already from the bare band anisotropy [Figs. 19(c′) and 19(d′)], which is however further enhanced by *d*FSD correlations as seen in Figs. 19(c) and 19(d).

*d*FSD correlations also provide a natural scenario to account for the observed enhanced anisotropy of $\mathrm{Im}\,\chi(\mathbf{q},\omega)$ in the pseudogap phase of underdoped $\mathrm{YBa_2Cu_3O_{6.6}}$.[55] As seen in Figs. 20(c), 20(c′), 20(d), and 20(d′), the anisotropy of $\mathrm{Im}\,\chi(\mathbf{q},\omega)$ is substantially enhanced compared with the bare anisotropy effect especially at relatively high temperatures. We note that the obtained anisotropy at high T in the left-hand panel of Fig. 20 may be underestimated in the present calculation since we have assumed an isotropic hopping amplitude of bosons $\langle b_{\mathbf{r}}^{\dagger} b_{\mathbf{r}'} \rangle = \delta$. Above the superconducting transition temperature, the bosons are not really condensed at the bottom of the band and $\langle b_{\mathbf{r}}^{\dagger} b_{\mathbf{r}'} \rangle$ can become anisotropic, contributing thus to an enhancement of the anisotropy of magnetic excitations.

Due to *d*FSD correlations, we can expect a relatively large anisotropy at low δ and high T in orthorhombic YBCO. A large anisotropy was actually reported in resistivity measurements a few yeas ago.[118] The data, however, were interpreted in terms of partial spin-charge stripe order, often referred to as (electronic) nematic order.[78] Although the nematic order has the same symmetry as the *d*FSD, namely orientational symmetry breaking of the square lattice, the underlying mechanism is different. *d*FSD correlations come from forward scattering processes of quasiparticles close to the FS near $(\pi,0)$ and $(0,\pi)$,[44,61] while a spin-charge stripe requires correlations with a large momentum transfer such as antiferromagnetism. Our scenario offers a different route to understand the anisotropy of the resistivity[118] as well as the anisotropy of the magnetic excitation spectrum[13,54,55] on the basis of a microscopic model calculation.

D. Fermi surface and superconducting gap anisotropy

Because of *d*FSD correlations, the FS of the antibonding band can easily open in the presence of a small bare band anisotropy as shown in Fig. 4. The Fermi surface topology depends in particular on the values of α and t_z/t. Further efforts to determine the FS shape in YBCO (Refs. 119 and 120) will serve to extract these parameters, which then gives insights on chain band effects as well as on the present scenario for the anisotropy of magnetic excitations. As shown in Fig. 5, the hole density of the antibonding band is significantly larger than that of the bonding band. This self-consistent result may be useful for mapping the FS in future ARPES studies.

Although the inner FS can change its topology with α, such a topology change does not strongly affect the anisotropy of $\mathrm{Im}\,\chi(\mathbf{q},\omega)$. We have not observed an enhanced $\Delta\eta$ when the inner FS opens, but a simple linear relation $\Delta\eta \propto \alpha$ in good approximation at low T for $\omega < \omega_{\mathbf{Q}}^{\mathrm{res}}$.

The present self-consistent calculation yields $\Delta_x > |\Delta_y|$ for $\alpha < 0$, that is, $\Delta_s > 0$ [Fig. 3(a)], which partially compensates the bare anisotropy of $J_{\mathbf{r}\mathbf{r}'}$ [see Eq. (5)]; note that Δ_τ is the RVB pairing amplitude and the true gap magnitude is given by $J_\tau \Delta_\tau$. Hence we obtain $J_x\Delta_x < |J_y\Delta_y|$ with an anisotropy a bit smaller than $|2\alpha|$, about 7% for $\delta = 0.10-0.20$ and $\alpha = -0.05$. The relation $J_x\Delta_x < |J_y\Delta_y|$ was actually reported in a Raman scattering experiment for the optimally doped and overdoped YBCO.[121] Note that this gap anisotropy does not lead to a gap anisotropy between $\mathbf{k} = (\pi,0)$ and $(0,\pi)$, which comes from Δ_z in the present theory, as seen from Eqs. (5) and (6). While the magnitude of Δ_z might look sizable in Fig. 3(c) especially for high δ, Δ_z is multiplied by J_z in Eq. (6). The resulting anisotropy between $\Delta_{\mathbf{k}=(\pi,0)}$ and $\Delta_{\mathbf{k}=(0,\pi)}$ becomes very small, less than 1% for our parameters. Recent ARPES data[120] reported an anisotropy of about 50%, which cannot be understood in the present model.

VI. CONCLUSION

We have performed a comprehensive analysis of the bilayer *t*-*J* model in the slave-boson mean-field scheme. After determining the mean fields self-consistently, we have calculated the dynamical magnetic susceptibility in a renormalized RPA. We have shown that prominent features of magnetic excitations of YBCO are captured by this scheme: (i) the IC and DIC signals only for $T < T_{\mathrm{RVB}}$, (ii) the collective mode for $T < T_{\mathrm{RVB}}$, (iii) its downward dispersion for $\omega \lesssim \omega_{\mathbf{Q}}^{\mathrm{res}}$, (iv) the δ dependence of $\omega_{\mathbf{Q}}^{\mathrm{res}}$, (v) the overdamped collective excitation for $\omega \gtrsim \omega_{\mathbf{Q}}^{\mathrm{res}}$ with an upward dispersion, (vi) robustness of this high energy dispersive feature to T, and (vii) spectral weight suppression of the even channel.

In particular, the present theory, which includes *d*FSD correlation effects in a self-consistent manner, provides a natural scenario to understand the observed anisotropy of Im $\chi(\mathbf{q},\omega)$: (i) appreciable anisotropy also for low δ, and (ii) enhanced anisotropy at relatively high T ($\sim T_{\mathrm{RVB}}$).

Although magnetic excitations of high-T_c cuprates are often discussed in terms of spin-charge stripes after the proposal by Tranquada *et al.*,[48] the present comprehensive study indicates that conventional particle-hole scattering processes around the FS are essential to magnetic excitations. An additional insight from this study is the importance of *d*FSD correlations for the anisotropy of Im $\chi(\mathbf{q},\omega)$. *d*FSD correlations are due to forward scattering interactions, which were so far ignored in most theories.

ACKNOWLEDGMENTS

The authors are grateful to O. K. Andersen, V. Hinkov, B. Keimer, D. Manske, and R. Zeyher for helpful discussions and for sharing some unpublished results with us.

---

[1] J. Rossat-Mignod, L. P. Regnault, C. Vettier, P. Bourges, P. Burlet, J. Bossy, J. Y. Henry, and G. Lapertot, Physica C **185-189**, 86 (1991).

[2] T. R. Thurston, R. J. Birgeneau, M. A. Kastner, N. W. Preyer, G. Shirane, Y. Fujii, K. Yamada, Y. Endoh, K. Kakurai, M. Matsuda, Y. Hidaka, and T. Murakami, Phys. Rev. B **40**, 4585 (1989).

[3] S.-W. Cheong, G. Aeppli, T. E. Mason, H. Mook, S. M. Hayden, P. C. Canfield, Z. Fisk, K. N. Clausen, and J. L. Martinez, Phys. Rev. Lett. **67**, 1791 (1991).

[4] T. E. Mason, G. Aeppli, and H. A. Mook, Phys. Rev. Lett. **68**, 1414 (1992).

[5] T. R. Thurston, P. M. Gehring, G. Shirane, R. J. Birgeneau, M. A. Kastner, Y. Endoh, M. Matsuda, K. Yamada, H. Kojima, and I. Tanaka, Phys. Rev. B **46**, 9128 (1992).

[6] P. Dai, H. A. Mook, and F. Doğan, Phys. Rev. Lett. **80**, 1738 (1998).

[7] J. M. Tranquada, P. M. Gehring, G. Shirane, S. Shamoto, and M. Sato, Phys. Rev. B **46**, 5561 (1992).

[8] B. J. Sternlieb, J. M. Tranquada, G. Shirane, M. Sato, and S. Shamoto, Phys. Rev. B **50**, 12915 (1994).

[9] H. A. Mook, P. Dai, S. M. Hayden, G. Aeppli, T. G. Perring, and F. Doğan, Nature (London) **395**, 580 (1998).

[10] M. Arai, T. Nishijima, Y. Endoh, T. Egami, S. Tajima, K. Tomimoto, Y. Shiohara, M. Takahashi, A. Garrett, and S. M. Bennington, Phys. Rev. Lett. **83**, 608 (1999).

[11] P. Bourges, Y. Sidis, H. F. Fong, L. P. Regnault, J. Bossy, A. Ivanov, and B. Keimer, Science **288**, 1234 (2000).

[12] P. Dai, H. A. Mook, R. D. Hunt, and F. Doğan, Phys. Rev. B **63**, 054525 (2001).

[13] C. Stock, W. J. L. Buyers, R. Liang, D. Peets, Z. Tun, D. Bonn, W. N. Hardy, and R. J. Birgeneau, Phys. Rev. B **69**, 014502 (2004).

[14] G. Aeppli, T. E. Mason, S. M. Hayden, H. A. Mook, and J. Kulda, Science **278**, 1432 (1997).

[15] H. A. Mook, M. Yethiraj, G. Aeppli, T. E. Mason, and T. Armstrong, Phys. Rev. Lett. **70**, 3490 (1993).

[16] P. Bourges, L. P. Regnault, J. Y. Henry, C. Vettier, Y. Sidis, and P. Burlet, Physica B **215**, 30 (1995).

[17] H. F. Fong, B. Keimer, P. W. Anderson, D. Reznik, F. Doğan, and I. A. Aksay, Phys. Rev. Lett. **75**, 316 (1995); H. F. Fong, B. Keimer, D. Reznik, D. L. Milius, and I. A. Aksay, Phys. Rev. B **54**, 6708 (1996).

[18] P. Bourges, L. P. Regnault, Y. Sidis, and C. Vettier, Phys. Rev. B **53**, 876 (1996).

[19] P. Dai, M. Yethiraj, H. A. Mook, T. B. Lindemer, and F. Doğan, Phys. Rev. Lett. **77**, 5425 (1996).

[20] H. F. Fong, B. Keimer, D. L. Milius, and I. A. Aksay, Phys. Rev. Lett. **78**, 713 (1997).

[21] D. Reznik, P. Bourges, L. Pintschovius, Y. Endoh, Y. Sidis, T. Masui, and S. Tajima, Phys. Rev. Lett. **93**, 207003 (2004).

[22] S. Pailhès, Y. Sidis, P. Bourges, V. Hinkov, A. Ivanov, C. Ulrich, L. P. Regnault, and B. Keimer, Phys. Rev. Lett. **93**, 167001 (2004).

[23] S. M. Hayden, H. A. Mook, P. Dai, T. G. Perring, and F. Doğan, Nature (London) **429**, 531 (2004).

[24] J. M. Tranquada, H. Woo, T. G. Perring, H. Goka, G. D. Gu, G. Xu, M. Fujita, and K. Yamada, Nature (London) **429**, 534 (2004).

[25] Q. Si, Y. Zha, K. Levin, and J. P. Lu, Phys. Rev. B **47**, 9055 (1993).

[26] T. Tanamoto, H. Kohno, and H. Fukuyama, J. Phys. Soc. Jpn. **62**, 717 (1993).

[27] T. Tanamoto, H. Kohno, and H. Fukuyama, J. Phys. Soc. Jpn. **63**, 2739 (1994).

[28] D. Z. Liu, Y. Zha, and K. Levin, Phys. Rev. Lett. **75**, 4130 (1995).

[29] J. H. Xu, T. J. Watson-Yang, J. Yu, and A. J. Freeman, Phys. Lett. A **120**, 489 (1987).

[30] J. Yu, S. Massidda, A. J. Freeman, and D. D. Koeling, Phys. Lett. A **122**, 203 (1987).

[31] K. T. Park, K. Terakura, T. Oguchi, A. Yanase, and M. Ikeda, J. Phys. Soc. Jpn. **57**, 3445 (1988).

[32] J. C. Campuzano, G. Jennings, M. Faiz, L. Beaulaigue, B. W. Veal, J. Z. Liu, A. P. Paulikas, K. Vandervoort, H. Claus, R. S. List, A. J. Arko, and R. J. Bartlett, Phys. Rev. Lett. **64**, 2308 (1990).

[33] R. Liu, B. W. Veal, A. P. Paulikas, J. W. Downey, P. J. Kostić, S. Fleshler, U. Welp, C. G. Olson, X. Wu, A. J. Arko, and J. J. Joyce, Phys. Rev. B **46**, 11056 (1992).

[34] J. Brinckmann and P. A. Lee, Phys. Rev. Lett. **82**, 2915 (1999).

[35] Y.-J. Kao, Q. Si, and K. Levin, Phys. Rev. B **61**, R11898 (2000).

[36] M. R. Norman, Phys. Rev. B **61**, 14751 (2000).

[37] O. Tchernyshyov, M. R. Norman, and A. V. Chubukov, Phys.

Rev. B **63**, 144507 (2001).

[38] J. Brinckmann and P. A. Lee, Phys. Rev. B **65**, 014502 (2002).

[39] J.-X. Li and C.-D. Gong, Phys. Rev. B **66**, 014506 (2002).

[40] A. P. Schnyder, A. Bill, C. Mudry, R. Gilardi, H. M. Ronnow, and J. Mesot, Phys. Rev. B **70**, 214511 (2004).

[41] A. Ino, C. Kim, T. Mizokawa, Z.-X. Shen, A. Fujimori, M. Takaba, K. Tamasaku, H. Eisaki, and S. Uchida, J. Phys. Soc. Jpn. **68**, 1496 (1999); A. Ino, C. Kim, M. Nakamura, T. Yoshida, T. Mizokawa, A. Fujimori, Z.-X. Shen, T. Kakeshita, H. Eisaki, and S. Uchida, Phys. Rev. B **65**, 094504 (2002).

[42] X. J. Zhou, T. Yoshida, S. A. Kellar, P. V. Bogdanov, E. D. Lu, A. Lanzara, M. Nakamura, T. Noda, T. Kakeshita, H. Eisaki, S. Uchida, A. Fujimori, Z. Hussain, and Z.-X. Shen, Phys. Rev. Lett. **86**, 5578 (2001).

[43] For a review of the slave-boson mean-field theory of the two-dimensional *t-J* model, see: H. Fukuyama, J. Phys. Chem. Solids **59**, 447 (1998). This theory was later extended by including the possibility of a *d*FSD (Ref. 44).

[44] H. Yamase and H. Kohno, J. Phys. Soc. Jpn. **69**, 332 (2000); **69**, 2151 (2000).

[45] H. Yamase and H. Kohno, J. Phys. Soc. Jpn. **70**, 2733 (2001).

[46] H. Yamase, J. Phys. Soc. Jpn. **71**, 1154 (2002).

[47] H. Yamase and H. Kohno, Phys. Rev. B **68**, 014502 (2003).

[48] J. M. Tranquada, B. J. Sternlieb, J. D. Axe, Y. Nakamura, and S. Uchida, Nature (London) **375**, 561 (1995).

[49] T. Niemöller, N. Ichikawa, T. Frello, H. Hünnefeld, N. H. Andersen, S. Uchida, J. R. Schneider, and J. M. Tranquada, Eur. Phys. J. B **12**, 509 (1999).

[50] N. Ichikawa, S. Uchida, J. M. Tranquada, T. Niemöller, P. M. Gehring, S.-H. Lee, and J. R. Schneider, Phys. Rev. Lett. **85**, 1738 (2000).

[51] M. Fujita, H. Goka, K. Yamada, and M. Matsuda, Phys. Rev. Lett. **88**, 167008 (2002).

[52] S. A. Kivelson, I. P. Bindloss, E. Fradkin, V. Oganesyan, J. M. Tranquada, A. Kapitulnik, and C. Howald, Rev. Mod. Phys. **75**, 1201 (2003).

[53] H. A. Mook, P. Dai, F. Doğan, and R. D. Hunt, Nature (London) **404**, 729 (2000).

[54] V. Hinkov, S. Pailhès, P. Bourges, Y. Sidis, A. Ivanov, A. Kulakov, C. T. Lin, D. Chen, C. Bernhard, and B. Keimer, Nature (London) **430**, 650 (2004).

[55] V. Hinkov, P. Bourges, S. Pailhès, Y. Sidis, A. Ivanov, C. T. Lin, D. Chen, and B. Keimer, cond-mat/0601048 (unpublished).

[56] I. Eremin and D. Manske, Phys. Rev. Lett. **94**, 067006 (2005); **96**, 059902(E) (2006). Here a few comments are useful to avoid possible confusions: (i) the anisotropic Fermi surfaces in the inset of Fig. 1 of that paper should be rotated by 90° to be consistent with the orientation underlying their Fig. 4(b); in addition $(\pi,0)$ in Fig. 2 should be replaced by $(0,\pi)$; (ii) the nominal anisotropy of 3% and 5% in that paper corresponds to $\alpha=-0.06$ and $\alpha=-0.1$ in our notation; (iii) the choice of parameters in that paper leads to a rather high doping of about 0.21 in the superconducting state.

[57] A. P. Schnyder, D. Manske, C. Mudry, and M. Sigrist, cond-mat/0510790 (unpublished).

[58] T. Zhou and J.-X. Li, Phys. Rev. B **69**, 224514 (2004); **72**, 134512 (2005).

[59] Y.-J. Kao and H.-Y. Kee, Phys. Rev. B **72**, 024502 (2005).

[60] M. Vojta, T. Vojta, and R. K. Kaul, cond-mat/0510448 (unpublished).

[61] C. J. Halboth and W. Metzner, Phys. Rev. Lett. **85**, 5162 (2000).

[62] B. Valenzuela and M. A. H. Vozmediano, Phys. Rev. B **63**, 153103 (2001).

[63] I. Grote, E. Körding, and F. Wegner, J. Low Temp. Phys. **126**, 1385 (2002).

[64] C. Honerkamp, M. Salmhofer, and T. M. Rice, Eur. Phys. J. B **27**, 127 (2002).

[65] A. Neumayr and W. Metzner, Phys. Rev. B **67**, 035112 (2003).

[66] H. Yamase, Phys. Rev. Lett. **93**, 266404 (2004).

[67] A. Miyanaga and H. Yamase, Phys. Rev. B **73**, 174513 (2006).

[68] W. Metzner, D. Rohe, and S. Andergassen, Phys. Rev. Lett. **91**, 066402 (2003).

[69] I. Khavkine, C.-H. Chung, V. Oganesyan, and H.-Y. Kee, Phys. Rev. B **70**, 155110 (2004).

[70] H. Yamase, V. Oganesyan, and W. Metzner, Phys. Rev. B **72**, 035114 (2005).

[71] L. Dell'Anna and W. Metzner, Phys. Rev. B **73**, 045127 (2006).

[72] I. J. Pomeranchuk, Sov. Phys. JETP **8**, 361 (1958).

[73] M. Inui, S. Doniach, P. J. Hirschfeld, and A. E. Ruckenstein, Phys. Rev. B **37**, 2320 (1988).

[74] T. Giamarchi and C. Lhuillier, Phys. Rev. B **43**, 12943 (1991).

[75] S. R. White and D. J. Scalapino, Phys. Rev. Lett. **80**, 1272 (1998); **81**, 3227 (1998).

[76] X.-G. Wen and P. A. Lee, Phys. Rev. Lett. **76**, 503 (1996).

[77] E. Cappelluti and R. Zeyher, Phys. Rev. B **59**, 6475 (1999).

[78] S. A. Kivelson, E. Fradkin, and V. J. Emery, Nature (London) **393**, 550 (1998).

[79] P. Bourges, in *The Gap Symmetry and Fluctuations in High-*T_c *Superconductors*, edited by J. Bok, G. Deutscher, D. Pavuna, and S. A. Wolf (Plenum, New York, 1998), Vol. B371 of NATO ASI Series.

[80] S. Pailhès, Y. Sidis, P. Bourges, C. Ulrich, V. Hinkov, L. P. Regnault, A. Ivanov, B. Liang, C. T. Lin, C. Bernhard, and B. Keimer, Phys. Rev. Lett. **91**, 237002 (2003).

[81] S. Pailhès, C. Ulrich, B. Fauqué, V. Hinkov, Y. Sidis, A. Ivanov, C. T. Lin, B. Keimer, and P. Bourges, cond-mat/0512634 (unpublished).

[82] P. Bourges, H. F. Fong, L. P. Regnault, J. Bossy, C. Vettier, D. L. Milius, I. A. Aksay, and B. Keimer, Phys. Rev. B **56**, R11439 (1997).

[83] P. Dai, H. A. Mook, S. M. Hayden, G. Aeppli, T. G. Perring, R. D. Hunt, and F. Doğan, Science **284**, 1344 (1999).

[84] H. F. Fong, P. Bourges, Y. Sidis, L. P. Regnault, J. Bossy, A. Ivanov, D. L. Milius, I. A. Aksay, and B. Keimer, Phys. Rev. B **61**, 14773 (2000).

[85] C. Stock, W. J. L. Buyers, R. A. Cowley, P. S. Clegg, R. Coldea, C. D. Frost, R. Liang, D. Peets, D. Bonn, W. N. Hardy, and R. J. Birgeneau, Phys. Rev. B **71**, 024522 (2005).

[86] B. Normand, H. Kohno, and H. Fukuyama, J. Phys. Soc. Jpn. **64**, 3903 (1995).

[87] O. K. Andersen, A. I. Lichtenstein, O. Jepsen, and F. Paulsen, J. Phys. Chem. Solids **56**, 1573 (1995).

[88] D. L. Feng, N. P. Armitage, D. H. Lu, A. Damascelli, J. P. Hu, P. Bogdanov, A. Lanzara, F. Ronning, K. M. Shen, H. Eisaki, C. Kim, J.-I. Shimoyama, K. Kishio, and Z. X. Shen, Phys. Rev. Lett. **86**, 5550 (2001).

[89] Y.-D. Chuang, A. D. Gromko, A. Fedorov, Y. Aiura, K. Oka, Yoichi Ando, H. Eisaki, S. I. Uchida, and D. S. Dessau, Phys. Rev. Lett. **87**, 117002 (2001).

[90] J. D. Jorgensen, B. W. Veal, A. P. Paulikas, L. J. Nowicki, G. W.

Crabtree, H. Claus, and W. K. Kwok, Phys. Rev. B **41**, 1863 (1990).

[91] L. F. Feiner, J. H. Jefferson, and R. Raimondi, Phys. Rev. Lett. **76**, 4939 (1996).

[92] T. Tohyama and S. Maekawa, Semicond. Sci. Technol. **13**, R17 (2000).

[93] E. Pavarini, I. Dasgupta, T. Saha-Dasgupta, O. Jepsen, and O. K. Andersen, Phys. Rev. Lett. **87**, 047003 (2001).

[94] M. S. Hybertsen, E. B. Stechel, M. Schluter, and D. R. Jennison, Phys. Rev. B **41**, 11068 (1990).

[95] S. M. Hayden, G. Aeppli, T. G. Perring, H. A. Mook, and F. Doğan, Phys. Rev. B **54**, R6905 (1996).

[96] D. Reznik, P. Bourges, H. F. Fong, L. P. Regnault, J. Bossy, C. Vettier, D. L. Milius, I. A. Aksay, and B. Keimer, Phys. Rev. B **53**, R14741 (1996).

[97] P. V. Bogdanov, A. Lanzara, X. J. Zhou, S. A. Kellar, D. L. Feng, E. D. Lu, H. Eisaki, J.-I. Shimoyama, K. Kishio, Z. Hussain, and Z. X. Shen, Phys. Rev. B **64**, 180505(R) (2001).

[98] O. K. Andersen (private communication).

[99] H. Yamase, H. Kohno, H. Fukuyama, and M. Ogata, J. Phys. Soc. Jpn. **68**, 1082 (1999).

[100] G. J. Chen, R. Joynt, F. C. Zhang, and C. Gros, Phys. Rev. B **42**, 2662 (1990).

[101] A. Himeda and M. Ogata, Phys. Rev. B **60**, R9935 (1999).

[102] M. Akoshima and Y. Koike, J. Phys. Soc. Jpn. **67**, 3653 (1998).

[103] N. Bulut and D. J. Scalapino, Phys. Rev. B **53**, 5149 (1996).

[104] A. V. Chubukov, B. Jankó, and O. Tchernyshyov, Phys. Rev. B **63**, 180507(R) (2001).

[105] F. Onufrieva and P. Pfeuty, Phys. Rev. B **65**, 054515 (2002).

[106] I. Eremin, D. K. Morr, A. V. Chubukov, K. Bennemann, and M. R. Norman, Phys. Rev. Lett. **94**, 147001 (2005).

[107] M. Lavagna and G. Stemmann, Phys. Rev. B **49**, 4235 (1994).

[108] G. Blumberg, B. P. Stojković, and M. V. Klein, Phys. Rev. B **52**, R15741 (1995).

[109] E. Demler, H. Kohno, and S.-C. Zhang, Phys. Rev. B **58**, 5719 (1998).

[110] C. D. Batista, G. Ortiz, and A. V. Balatsky, Phys. Rev. B **64**, 172508 (2001).

[111] I. F. Herbut and D. J. Lee, Phys. Rev. B **68**, 104518 (2003).

[112] A. J. Millis and H. Monien, Phys. Rev. B **54**, 16172 (1996).

[113] T. Dahm, D. Manske, and L. Tewordt, Phys. Rev. B **58**, 12454 (1998); D. Manske, I. Eremin, and K. H. Bennemann, *ibid.* **63**, 054517 (2001).

[114] I. Sega, P. Prelovšek, and J. Bonča, Phys. Rev. B **68**, 054524 (2003); I. Sega and P. Prelovšek, Phys. Rev. B **73**, 092516 (2006).

[115] Y. Zha, K. Levin, and Q. Si, Phys. Rev. B **47**, 9124 (1993).

[116] V. Hinkov (private communication).

[117] A. Damascelli, Z. Hussain, and Z. X. Shen, Rev. Mod. Phys. **75**, 473 (2003).

[118] Y. Ando, K. Segawa, S. Komiya, and A. N. Lavrov, Phys. Rev. Lett. **88**, 137005 (2002).

[119] M. C. Schabel, C.-H. Park, A. Matsuura, Z.-X. Shen, D. A. Bonn, R. Liang, and W. N. Hardy, Phys. Rev. B **57**, 6107 (1998).

[120] D. H. Lu, D. L. Feng, N. P. Armitage, K. M. Shen, A. Damascelli, C. Kim, F. Ronning, Z.-X. Shen, D. A. Bonn, R. Liang, W. N. Hardy, A. I. Rykov, and S. Tajima, Phys. Rev. Lett. **86**, 4370 (2001).

[121] M. F. Limonov, A. I. Rykov, S. Tajima, and A. Yamanaka, Phys. Rev. B **61**, 12412 (2000).